

# **Underwater wide field tomography of sediment resuspension**

**Adi Vainiger**



# **Underwater wide field tomography of sediment resuspension**

Research Thesis

Submitted in partial fulfillment of the requirements  
for the degree of Master of Science in Electrical Engineering

**Adi Vainiger**

Submitted to the Senate  
of the Technion — Israel Institute of Technology  
Tishrei 5800      Haifa      October 2019



This research was carried out under the supervision of Prof. Yoav Y. Schechner in the Andrew and Erna Viterbi Faculty of Electrical Engineering.

## Publications

Some results in this thesis have been published as articles by the author and research collaborators in conferences and journals during the course of the author's master research period, the most up-to-date versions of which being:

- Adi Vainiger, Yoav Y. Schechner, Tali Treibitz, Aviad Avni, and David S. Timor, "Underwater Wide-Field Tomography of Sediment Resuspension", in Particles in Europe conference 2018, (2018).
- Adi Vainiger, Yoav Y. Schechner, Tali Treibitz, Aviad Avni, and David S. Timor, "Optical wide-field tomography of sediment resuspension," *Optics Express* 27, A766-A778 (2019).

## Acknowledgements

I especially thank Prof. Yoav Y. Schechner, for being much more than an advisor, a mentor that made the road both challenging and enjoyable.

I thank Dr. Tali Treibitz and Aviad Avni from The Leon H. Charney School of Marine Sciences, University of Haifa, as well as David S. Timor, for their fruitful cooperation, and great contribution to the building of the Tomography system and conducting the experiments. I am grateful to those who assisted in the system construction and experiments Michael Fisher, Ido Czerninski, Yuval Goldfracht, Leonid Dehter, Ben Herzberg, Assaf Levy, Judith Fischer, Prof. Morel Groper, Samuel Cohen, and Sharon Farber.

I thank my colleagues for the fruitful discussions, and helpful feedback, Vadim Holodovsky, Aviad Levis, Dr. Amit Aides, Lior Arbel, Dr. Masada Tzemach Tzabari, and Mark Sheinin from the Hybrid Imaging Laboratory, The Andrew and Erna Viterbi Faculty of Electrical Engineering.

For technical support I thank Ina Talmon and Johanan Erez from The Vision and Image Sciences Laboratory, Roy Mitarany from the Networked Software Systems Laboratory, The Andrew and Erna Viterbi Faculty of Electrical Engineering, Technion. For technical guidance and tools used during sediment calibration and validation, I thank Galia Ben-David from the Stem Cell and Tissue Engineering Laboratory, The Faculty of Biomedical Engineering, Technion.

I am grateful of the fruitful discussions with our research collaborators, Dr. Timor Katz from the Israel Oceanographic and Limnological Research, Prof. Gitay Yahel and Merav Gilboa from Oceanography and Marine Biology, Ruppin Academic Center, and Prof. Uri Shavit and Shachar Grossbard from the Civil and Environmental Engineering, Technion.

The research for this thesis was mainly conducted in the Ollendorff Minerva Center. Minerva is funded through the BMBF. During my studies, I received support from The US-Israel Binational Science Foundation (BSF), MAFA'T, and The Israeli Ministry of Science, Technology, and Space (MOST).

The generous financial help of the Technion is gratefully acknowledged.

# Contents

<b>Abstract</b>	<b>1</b>
<b>Abbreviations</b>	<b>3</b>
<b>Notations</b>	<b>5</b>
<b>1 Introduction</b>	<b>9</b>
<b>2 Literature survey</b>	<b>11</b>
<b>3 Theoretical modeling</b>	<b>15</b>
3.1 Image formation model . . . . .	15
3.2 Tomographic reconstruction - inverse model . . . . .	16
3.3 SART . . . . .	18
<b>4 Design of the electro-optical tomography setup</b>	<b>21</b>
4.1 System requirements . . . . .	21
4.2 Imaging spatial resolution . . . . .	22
4.3 Light screen intensity . . . . .	25
<b>5 Simulations</b>	<b>29</b>
5.1 Renderings . . . . .	29
5.2 Simulated tomographic reconstructions . . . . .	30
<b>6 Tomographic experiments</b>	<b>33</b>
6.1 System and method . . . . .	33
6.2 Tomography reconstructions . . . . .	34
6.3 Sediment density calibration . . . . .	36
6.4 Injection system validation . . . . .	38
<b>7 Discussion and outlook</b>	<b>41</b>
<b>Hebrew Abstract</b>	<b>i</b>



# List of Figures

1.1	Visualization of underwater in-situ optical-CT of sediment resuspension.	9
1.2	Biological resuspension events.	10
2.1	In-situ sensors mounted on a mooring system.	12
2.2	Particle imaging velocimetry systems.	13
2.3	Tomographic shadowgraphy.	14
2.4	Cloud CT	14
3.1	The concept of an underwater optical tomography system	16
4.1	Visualization of imaging requirements	22
4.2	Spatial resolution specifications of the imagine system	23
4.3	Flat port and <i>Snell's law</i>	23
4.4	Circle of confusion diameter as a function of distance	24
4.5	Modulation Transfer Function	25
4.6	The radiance excitation of screen	26
4.7	Quantum Efficiency of camera	28
5.1	Simulations process	31
6.1	Tomographic system design	34
6.2	Tomographic system images	34
6.3	Experiment - process and reconstruction	35
6.4	Experiment - mass reconstruction	36
6.5	Experiment - scattered signal of cloud	36
6.6	Sediment calibration system	37
6.7	Sediment calibration results	38
6.8	Injection system validation	39



# List of Tables

4.1 Imaging requirements . . . . .	22
------------------------------------	----



# Abstract

Sediment resuspension is the transport of previously settled particles from the seafloor back into the overlying water. Sediment resuspension affects processes in nature as nutrients recycling and water quality. There is a gap of knowledge of biological sediment resuspension events, stems from a lack in methods to quantify them and estimate their effects on the environment. Measuring these abrupt and spatially varying events is challenging. Existing in-situ approaches are very localized.

We present a novel wide-field imaging approach to optically sense underwater sediment resuspension events from a distance. It uses wide-field multi-directional views and diffuse backlight. Our approach algorithmically quantifies the amount of material resuspended and its spatiotemporal distribution in three-dimensions (3D). The suspended particles affect the radiation that reaches the cameras, hence the captured images. By measuring the radiance during and prior to resuspension, we extract the optical depth on the line of sight (LOS) per pixel. Using computed tomography (CT) principles, the optical depths yield estimation of the extinction coefficient of the suspension, per voxel. The suspended density is then derived from the reconstructed extinction coefficient.

This thesis elaborates on the concept of the proposed approach, including a theoretical formulation, computer simulations, engineering of an optical CT system, algorithm and empirical validation results.



# Abbreviations

Abbreviation	Meaning
1D	One dimensional
2D	Two dimensional
3D	Three dimensional
CoC	Circle of Confusion
CT	Computed Tomography
DoF	Depth of Field
FoV	Field of View
fps	Frames per second
HG	Henyey-Greenstein
IR	Infra-Red
LED	Light Emitting Diode
LOS	Line Of Sight
lp	Line pairs
MTF	Modulation transfer function of a lens
PIV	Particle Imaging Velocimetry
QE	Quantum Efficiency
RGB	Red, Green, and Blue optical color channels
SART	Simultaneous Algebraic Reconstruction Technique
Tomo-PIV	Tomographic PIV
UOV	Underwater Observation Volume



# Notations

Notation	Meaning
$\mathbf{A}$	Projection lengths matrix from $n$ voxels to $m$ pixels in the scene
$\tilde{\mathbf{A}}$	A row-extended matrix of $\mathbf{A}$ , for solving a regularized problem
$a_{p,v}$	Length of ray segment of $\text{LOS}_p$ , in voxel $v$
$\tilde{a}_{q,v}$	Element of matrix $\tilde{\mathbf{A}}$
$\tilde{a}_q, \tilde{a}_v$	Row and column sums of $\tilde{\mathbf{A}}$ , respectively
$\alpha$	Regularization parameter of tomography optimization term
$b$	Relation coefficient between $\beta_v^{\text{Sed}}$ to $\rho_v^{\text{Mass}}$
$\beta^{\text{Sed}} = \{\beta_v^{\text{Sed}}\}_{v=1}^n$	The discretized volumetric extinction coefficient of the sediment cloud
$\beta^{\text{Sed}}(\mathbf{X})$	The volumetric extinction coefficient of the sediment cloud
$\beta^{\text{Water}}$	Extinction coefficient of water
$\beta_S^{\text{Water}}, \beta_A^{\text{Water}}$	Scattering and absorption coefficients of water
$c$	Speed of light
$\mathcal{C}$	Convex box constraint of a regularized problem
$\mathbf{D}_{\text{row}}, \mathbf{D}_{\text{col}}$	Diagonal matrices, defined as row and column sums of $\tilde{\mathbf{A}}$ , respectively.
$\Delta_{\text{lens}}$	The effective lens aperture diameter
$\Delta_{\text{object}}$	The diameter of blurred circle on the object/focus plane
$\Delta_{\text{pix}}$	The length side of a pixel
$\Delta_{\text{sensor}}$	The diameter of a projected circle on the sensor plane
$\Delta_{\text{UOV}}$	Length side of the UOV
$e^-$	Electrons count
$E_p$	The measured irradiance at pixel $p$ in Watts per meter square
$\epsilon_2$	Mean square error
$f$	Focal length of the camera
$f_{\text{CCD}}$	The distance of the sensor plane from the lens plane
$f_{\text{effective}}$	The effective optical length of the camera
$f_{\#}$	F-number of the camera lens
$g_{\text{HG}}$	Anisotropy parameter of a HG scattering phase function
$\gamma_e$	Number of photo-electrons per camera gray level
$h$	The Planck constant
$i$	Radiance intensity
$i_e$	Noisy pixel intensity in $[e^-]$

Notation	Meaning
$i_p$	Sediment suspension measurement at pixel $p$
$i_p^{(0)}$	Initial radiance emitted of the screen, corresponding to pixel $p$
$i_p^{\text{Ambient}}$	Ambient illumination radiance measured at pixel $p$
$i_p^{\text{Water}}$	Sediment-free water measurement at pixel $p$
$i_{\text{rec}}$	Averaged intensity inside a rectangle measuring clear water
$i_{\text{rec}}^{\text{Water}}$	Averaged intensity inside a rectangle measuring sediment suspension
$J_p^{\text{rad}}, J_p^e$	Radiometric and electric pixel energy in Joules
$J_{\text{photon}}^{\lambda}$	The energy of a photon in wavelength $\lambda$ in Joules
$k$	Step number of SART optimization process
$l$	Inner diameter of the beaker
$\mathcal{L}_{\text{screen}}$	The radiant power of the screen in Lumens
$\mathcal{L}$	3D Laplacian operator
$\lambda$	Wavelength in nm
$\text{LOS}_p$	LOS corresponding to pixel $p$
$m$	Number of pixels in the scene
$M$	The emitted radiance exitance in Watts per meter square
$\mu_{\text{total}}^{\text{Sed}}$	Total mass of sediment particles cloud
$\mu_v^{\text{Sed}}$	Mass of sediment particles per voxel $v$
$n$	Total number of voxels in the scene
$N_{\text{photons}}^{\lambda}$	The number of photons in wavelength $\lambda$ , generating electrons
$N_{\text{views}}$	Number of cameras observing the scene
$n_{\text{Water}}, n_{\text{Air}}$	The refractive indices of the water and air, respectively
$N_{\text{Well}}$	The number of electrons in a pixel during saturation state
$N_{\text{width}} \times N_{\text{height}}$	Resolution of camera sensor
$\nu_e^P$	Photon signal generated by Monte-Carlo simulations
$\omega$	A solid angle in screen plane in Steradians
$p$	Index of a pixel
$\mathcal{P}_{\mathcal{C}}$	An orthogonal projection on the convex set of box constraint $\mathcal{C}$
$\Phi_{\text{screen}}$	The radiant power of the screen in Watts
$\text{QE}^{\lambda}$	The QE of sensor response to arriving photons at wavelength $\lambda$
$\rho_v^{\text{Mass}}$	Mass density of sediment particles per voxel $v$
$\rho_v^{\#}$	Number density of sediment particles per voxel $v$
$S_p$	Surface area of pixel $p$
$S_{\text{screen}}$	Surface area of the lighting screen
$\sigma$	Extinction cross section of particles in the medium
$\sigma_{\text{read.e}}$	Camera read noise in electrons count
$T_{\text{diffuser}}$	The transmission efficiency of the screen diffusing layer
$t_{\text{exp}}$	Camera exposure time
$\tau_p$	Optical depth measured at pixel $p$
$\boldsymbol{\tau} = \{\tau_p\}_{p=1}^m$	A vector representation of all measured optical depths in the scene

Notation	Meaning
$\tilde{\tau}$	A row-extended vector of $\tau$ , for solving a regularized problem
$\theta, \theta_{\text{Water}}$	Angles in degrees
$v$	Index of a voxel
$\varpi^{\text{Water}}$	Single scattering albedo of water
$\vartheta$	Volume of a voxel
$X$	Positions in $\mathbb{R}^3$ space
$Z$	Working distance from the observed cloud
$Z_f, Z_r$	The forward and rear margins of the DoF, respectively



# Chapter 1

## Introduction

We propose an approach for underwater in-situ optical-computed tomography (CT). It is aimed for the study of marine sedimentation (Fig. 1.1). Sedimentation affects physical, chemical, and biological processes in the sea [1–3]. Among these processes are nutrient recycling, sediment transport, water quality, and dispersion of pollutants.

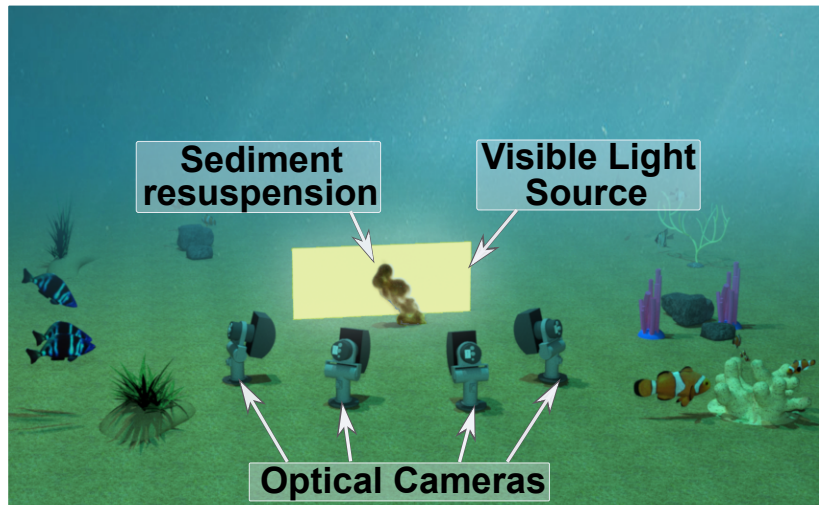


Fig. 1.1. Visualization of an underwater in-situ optical-computed tomography

Marine sediments contain particles of different sizes and originate from broken-down rocks or decomposed organic materials. One sedimentation process is resuspension of sediments, which manifests as an evolving underwater sand cloud. Such an event occurs when near seafloor currents exceed threshold velocity. The currents are induced by physical forces, such as waves, winds or tides; human activities, such as fishing, dredging and trawling; and biological activity. Biological resuspension (Fig. 1.2) occurs when fish and other animals search for food and shelter at the seafloor.

There is a gap of knowledge regarding the rate and extent of biological sediment resuspension in the ocean [4]. Moreover, the relevance of biological sediment resuspension to biochemical underwater processes is not fully known. Recent publications suggest that due to its frequent occurrences, biological activity may be a more significant



Fig. 1.2. Biological resuspension events: Fish and animals resuspend sediment while searching for food and shelter at the seafloor. Photos credits : Prof. Gitai Yahel and Merav Gilboa, The School of Marine Sciences, Ruppin Academic Center, Michmoret, Israel. More videos are available at [9–11]

contributor to sediment resuspension than physical forces and human activity [5–8]. Due to these reasons it is important to devise methods for measuring these events. However, this is challenging due to the sporadic and intense nature of fish movement [4, 12, 13]. Understanding resuspension requires a wide set of methods [4, 11, 14, 15]. Existing in-situ approaches for quantifying sediment resuspension or fluids are very localized and limited to cm-scale [16–19].

We seek methods that less disrupt resuspension events, hence we seek measurements from a distance. In aquatic environments, a sensing range of several meters is practical. In addition, the evolving sediment clouds have a meter-scale as well. Therefore, we seek multi-meter-scale far-field measurements of these events using cameras. The presented imaging approach (a) observes from a distance the water medium above the seafloor, (b) senses sediment resuspension events, and (c) algorithmically quantifies the resuspension. The spatial distribution of the particles is three-dimensional (3D). Hence, we develop a 3D tomographic imaging system. To achieve this, the evolving sediment cloud is imaged against a diffuse back-light. Imaging is done simultaneously from multiple directions and locations (Figs. 1.1 and 3.1). The resuspended particles affect the light that reaches the cameras. Image analysis uses a CT principle, motivated by medical CT.

In a small scale, optical CT was used in a laboratory studies on the dynamics of fluids and particles [20–23], and a recent in-situ study of marine microscopic and mesoscopic organisms [24]. Recently, CT has expanded to large-scale 3D atmospheric sensing of aerosols and clouds [25–27]. This work proposes a meter-scale CT to optically quantify underwater resuspension. We develop optical and algorithmic techniques to function through challenges posed by the underwater environment [28–31]. Initial partial results of our work have been presented in [32].

# Chapter 2

## Literature survey

This chapter provides an overview of existing literature on in-situ measurement of marine sedimentation, laboratory study of fluids and particles, and 3D atmospheric sensing of aerosols and clouds. Several ideas were drawn from these works and were incorporated into our work, such as the mathematical retrieval model, the system calibration, and CT.

There are numerous in-situ methods for measuring the marine environment. Here, we focus on optical and acoustical methods related to marine sedimentation. Most in-situ optical sensors measure the inherent optical properties of water. These sensors usually include active light sources, and they measure different parts of the volume scattering function. The volume scattering function is an inherent optical property describing the propagation of light in water. This function varies with angular direction and wavelength, and is influenced by concentration, size and shape of particles in the water [33, 34].

Turbidity sensors measure the scattered light intensity from the suspended particles and indicate their concentration [35, 36]. Some measure around an angle of 90° from the transmitted beam. Optical back-scattering sensors measure infra-red (IR) light scattered typically between 115° and 145°. The sampled volume is relatively small, up to a few cm across, depending on penetration depth of the IR beam. Turbidity sensors usually require extensive efforts of calibration. Optical Laser diffraction instruments as the Laser In-Situ Scattering and Transmissometry [37, 38], measure multiple angles of scattering, and yield particle size distribution and concentration of suspended sediments. The measurement volume resides within the instrument.

Acoustic in-situ methods measure particles' velocity in a remotely sampled volume, based on *Doppler shift* [39]. A typical acoustic Doppler velocimetry has a cylindrical sampling volume of 0.25 [mL], distant 5–10 [cm] from the tip of the transmitter, and 3–4 receivers. The receivers measure particles' velocity components. This method is sensitive to noise induced by various disturbances as turbulent fluctuations [40].

The sensors above are usually mounted on a mooring system deployed vertically underwater from a grounded anchor to a buoy (Fig. 2.1). The mooring systems combine

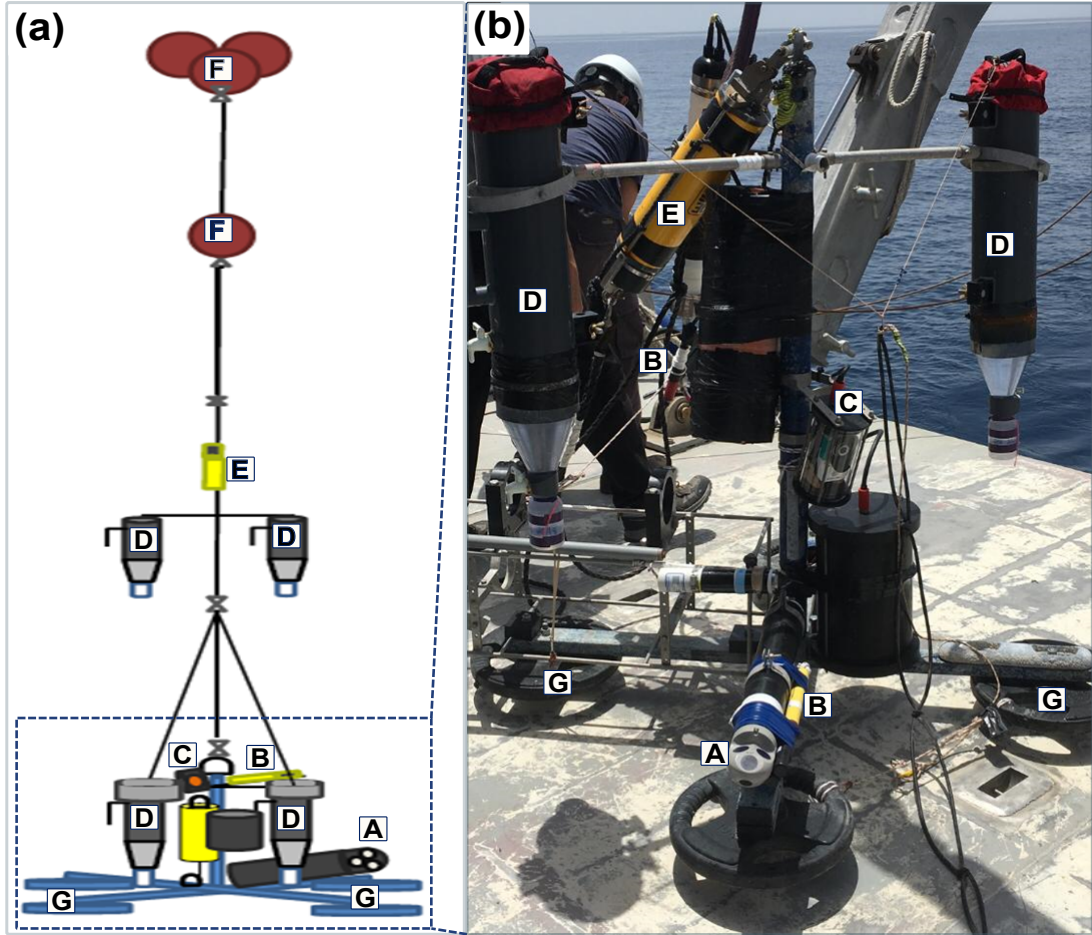


Fig. 2.1. (a) A diagram of in-situ sensors mounted on an underwater mooring system, containing: A. Acoustic Doppler Current Profiler; B. Optical Back Scatter sensors; C. A trap camera; D. Sediment traps; E. Acoustic Doppler Velocimetry; F. Buoys; G. Anchors. (b) Image of the lower part of the mooring system. Image and diagram credits: Merav Gilboa [11]

various sensors sets and sediments traps, to indicate the dynamics of sediments in the site [4, 6, 11, 14, 17, 41, 42].

A laboratory concept to measure and visualize the velocities of fluids is particle imaging velocimetry (PIV) [22]. The velocity is estimated indirectly by sensing small tracer particles that are seeded in the fluid and follow its dynamics. A typical PIV apparatus consists a camera synchronized to a strobe or laser. The system injects seeding particles to the investigated fluid. The camera measures the light scattered by the seeded particles. The measurement is limited to an illuminated area or volume, ranging from a few  $\mu\text{m}$  to several cm across. For a two dimensional (2D) illumination sheet, the approach uses cross-correlation to estimate the two-component velocity vector within small interrogation areas. For higher particle density, the method may fail, whereas for a low-density the setup is used for the study of individual particles' dynamics, known as particle tracking velocimetry [43, 44].

Recent developments brought PIV to in-situ oceanographic studies [45–48]. Other

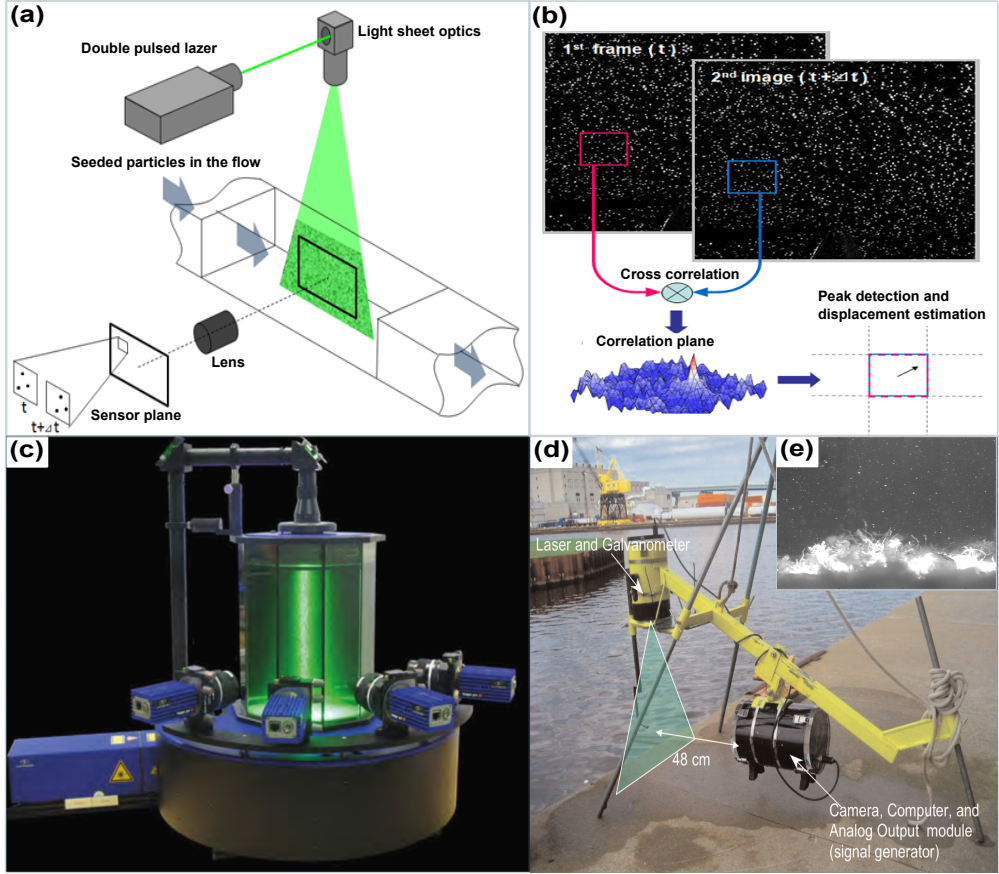


Fig. 2.2. (a) PIV Optical setup [57]. (b) Displacement and velocity evaluation of PIV [57]. (c) Tomo-PIV setup of *LaVision* [58]. (d) An in situ underwater PIV system [45], and (e) a sampled PIV image [45].

variants of PIV include two–four cameras and a 3D illuminating region. Tomographic PIV (Tomo-PIV) [20, 49–51] uses algebraic reconstruction techniques to estimate a three-component velocity vector of the fluid or to reconstruct the dynamics of injected droplets [52]. Tomographic shadowgraphy uses a similar setup to the one used in Tomo-PIV but measures the direct transmitted signal through the fluid without seeded particles. This approach reconstructs the 3D distribution of an injected liquid spray or the velocity of bubbles in fluid, using light sources as laser-induced fluorescence [53, 54], light emitting diodes (LED) [21, 23, 55] or X-Rays [56].

Another domain to which CT was recently introduced is the study of aerosols and clouds in the atmosphere. In [25], the authors showed that it is possible to reconstruct the 3D distribution of aerosols based on the single-scattering approximation, using scattering tomography. The image formation model is based on 3D radiative transfer. The single-scattering approximation is valid when the aerosols are very diluted. This simplifies both image formation and 3D reconstructing. For most clouds, however, single-scattering is not a valid approximation, thus multiple-scattering should be considered. Ref [59], presents an algorithm that achieves 3D reconstruction under multiple scattering. The method was developed for remote sensing from satellites or high flying airplanes

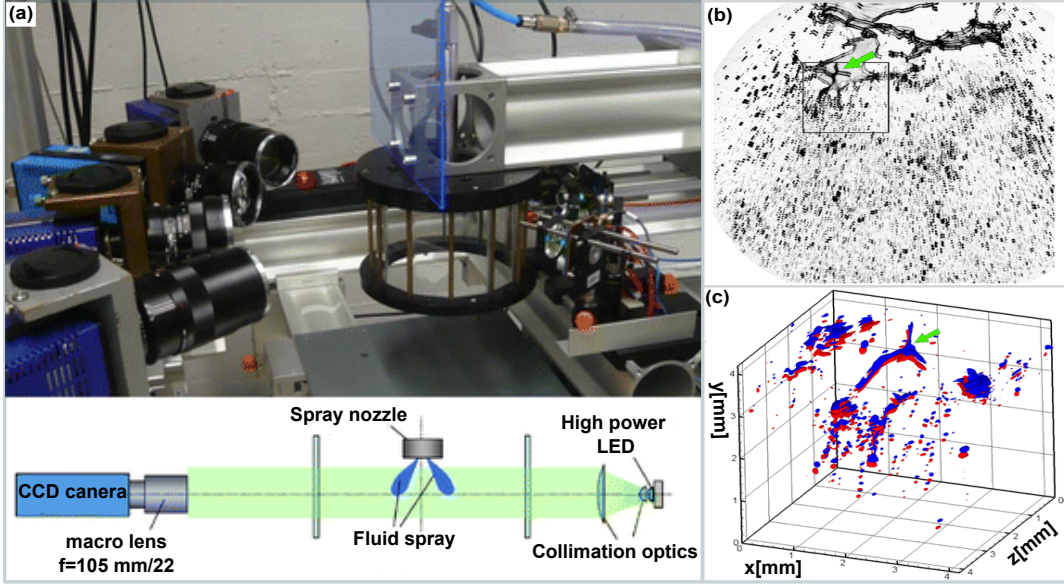


Fig. 2.3. (a) Tomographic shadowgraphy system [51]. (b) Shadowgraph image pair of the liquid spray. (c) Tomographic reconstruction of the sprayed liquid using back-projected images taken from four cameras. Blue represents the first reconstruction, red is the reconstruction 6.3[ $\mu$ sec] later. Images credit [51].

(Fig. 2.4). Introducing arbitrary scattering to tomography analysis using Monte Carlo was done in [27]. The method was tested on simulated images of in-situ ground-based cameras observing the scattering media in the atmosphere. The works above assume that the microphysical characteristics of the media are already known. Ref [60], suggests a method based on multi-spectral measurements, to assist reconstructing of the microphysics of scattering particles, such as their effective radius.

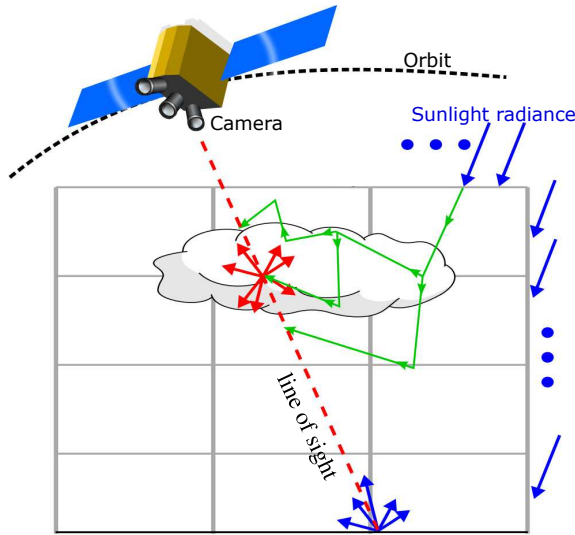


Fig. 2.4. Cloud CT [59].

# Chapter 3

## Theoretical modeling

### 3.1 Image formation model

When a scene is only under ambient illumination, the image measures radiance  $i_p^{\text{Ambient}}$  per pixel  $p$ . An active illumination screen has radiance  $i_p^{(0)}$ . Pixel  $p$  corresponds to a line of sight denoted  $\text{LOS}_p$ , see Fig. 3.1. The extinction coefficient of bulk water at the site is assumed to be spatially homogeneous. It is denoted as  $\beta^{\text{Water}}$  in units of  $[\text{m}^{-1}]$ . For sediment-free water, according to Beer-Lambert law, the transmitted radiance reaching  $p$  is<sup>1</sup>

$$i_p^{\text{Water}} \triangleq i_p^{(0)} \exp \left[ - \int_{\mathbf{X} \in \text{LOS}_p} \beta^{\text{Water}} d\mathbf{X} \right] + i_p^{\text{Ambient}} \quad \left[ \frac{\text{W}}{\text{m}^2 \cdot \text{sr}} \right]. \quad (3.1)$$

The attenuation of transmitted radiance is induced by absorption and scattering of light. Therefore, the water extinction coefficient satisfies

$$\beta^{\text{Water}} \triangleq \beta_A^{\text{Water}} + \beta_S^{\text{Water}} \quad [\text{m}^{-1}], \quad (3.2)$$

where  $\beta_S^{\text{Water}}$  and  $\beta_A^{\text{Water}}$  are the scattering and absorption coefficients of the water, respectively. The relative intensity of light scattered in a single scattering event is represented by the single scattering albedo

$$\varpi^{\text{Water}} \triangleq \frac{\beta_S^{\text{Water}}}{\beta_A^{\text{Water}} + \beta_S^{\text{Water}}}. \quad (3.3)$$

Let  $\beta^{\text{Sed}}(\mathbf{X})$  be the volumetric extinction coefficient of suspended sediment particles. Then the radiance measured through the suspension is

$$i_p = i_p^{(0)} \exp \left[ - \int_{\mathbf{X} \in \text{LOS}_p} \left( \beta^{\text{Water}} + \beta^{\text{Sed}}(\mathbf{X}) \right) d\mathbf{X} \right] + i_p^{\text{Ambient}} \quad \left[ \frac{\text{W}}{\text{m}^2 \cdot \text{sr}} \right]. \quad (3.4)$$

---

<sup>1</sup>Off-axis scattering affects the images. In preliminary lab experiments, these off-axis scattering components were significantly lower than the model in Eq. (3.1).

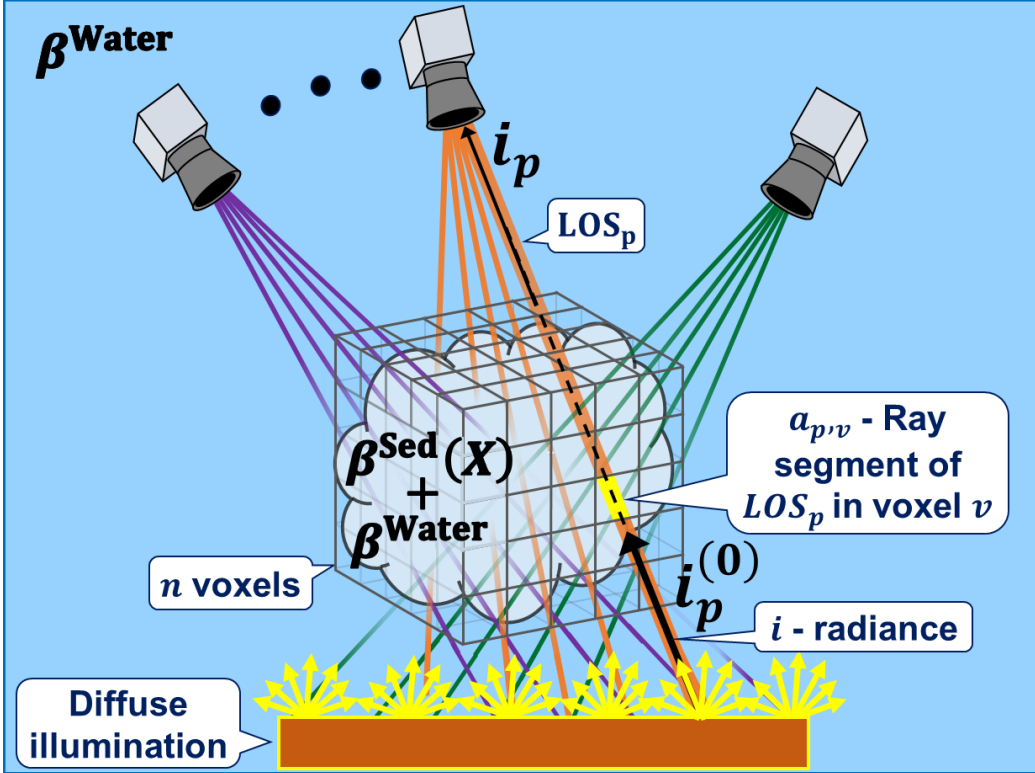


Fig. 3.1. The concept of an underwater optical tomography system. The volume includes water and a resuspended sediment cloud. There are  $n$  voxels. A line of sight corresponding to pixel  $p$  is  $\text{LOS}_p$ .

The unitless sediment optical depth at pixel  $p$  is

$$\tau_p \triangleq \int_{\mathbf{X} \in \text{LOS}_p} \beta^{\text{Sed}}(\mathbf{X}) d\mathbf{X}. \quad (3.5)$$

### 3.2 Tomographic reconstruction - inverse model

From measurements of  $i_p^{\text{Ambient}}$ ,  $i_p^{\text{Water}}$ ,  $i_p$ , and Eqs. (3.1), (3.4) and (3.5), the estimated optical depth per pixel  $p$  is

$$\tau_p = -\ln \left( \frac{i_p - i_p^{\text{Ambient}}}{i_p^{\text{Water}} - i_p^{\text{Ambient}}} \right). \quad (3.6)$$

Let  $a_{p,v}$  be the length [m] of ray segment of  $\text{LOS}_p$ , in voxel  $v$ , as noted in Fig. 3.1. Let  $\beta_v^{\text{Sed}}$  be the sediment extinction coefficient of voxel  $v$ . The vector  $\beta^{\text{Sed}} \in \mathbb{R}^{n \times 1}$  represents the extinction coefficients of all voxels  $v \in 1..n$ , in a column-stack form. A finite-sum approximation of Eq. (3.5) is

$$\tau_p \approx \sum_v a_{p,v} \beta_v^{\text{Sed}} \triangleq \mathbf{a}_p \cdot \boldsymbol{\beta}^{\text{Sed}}. \quad (3.7)$$

Tomographic setups have multidirectional LOSs through the scene, Fig. 3.1. Let  $N_{\text{views}}$  cameras observe the scene, each having resolution of  $N_{\text{width}} \times N_{\text{height}}$  pixels. The total number of pixels observing the scene is  $m = N_{\text{views}} \times N_{\text{width}} \times N_{\text{height}}$ . Then,  $\boldsymbol{\tau} \in \mathbb{R}^{m \times 1}$  represents the sampled optical depths in all pixels  $p \in 1..m$ . Define  $\mathbf{A} \in \mathbb{R}_+^{m \times n}$  as a projection matrix, whose elements are  $a_{p,v}$ . Then,

$$\boldsymbol{\tau} \approx \mathbf{A}\boldsymbol{\beta}^{\text{Sed}}. \quad (3.8)$$

Let  $\alpha \geq 0$  be a regularization parameter, and  $\mathcal{L}$  be a 3D Laplacian operator which defines the smoothness term of  $\boldsymbol{\beta}^{\text{Sed}}$ . Then the volumetric extinction coefficient can be estimated by:

$$\hat{\boldsymbol{\beta}}^{\text{Sed}} \triangleq \arg \min_{\boldsymbol{\beta}^{\text{Sed}}} \left( \left\| \mathbf{A}\boldsymbol{\beta}^{\text{Sed}} - \boldsymbol{\tau} \right\|_2^2 + \alpha \left\| \mathcal{L}\boldsymbol{\beta}^{\text{Sed}} \right\|_2^2 \right) \quad s.t. \quad \boldsymbol{\beta}^{\text{Sed}} \geq 0. \quad (3.9)$$

The extinction of light depends on the density and optical properties of the suspended particles. Sediment particles in the medium have an extinction cross section  $\sigma$  in units of  $[\text{m}^2]$ . Per voxel  $v$ , the number and mass densities of sediment particles are  $\rho_v^\#$  in units of  $[\frac{1}{\text{m}^3}]$  and  $\rho_v^{\text{Mass}}$  in units of  $[\frac{\text{gr}}{\text{m}^3}]$ , respectively. Each voxel has volume  $\vartheta$  in units of  $[\text{m}^3]$ . The mass of suspended particles in  $v$  is then

$$\mu_v^{\text{Sed}} = \rho_v^{\text{Mass}} \vartheta \quad [\text{gr}]. \quad (3.10)$$

The extinction coefficient is

$$\beta_v^{\text{Sed}} = \sigma \rho_v^\# \quad [\text{m}^{-1}]. \quad (3.11)$$

The particle mass density  $\rho_v^{\text{Mass}}$  is linearly proportional to particle number density  $\rho_v^\#$ . Thus, from Eq. (3.11) there is a linear relation between  $\beta_v^{\text{Sed}}$  and  $\rho_v^{\text{Mass}}$

$$\beta_v^{\text{Sed}} \triangleq b \rho_v^{\text{Mass}} \quad [\text{m}^{-1}]. \quad (3.12)$$

The coefficient  $b$  in units of  $[\frac{\text{m}^2}{\text{gr}}]$  can be calibrated (See Section 6.3). From Eqs. (3.10) and (3.12) the estimated mass of suspended particles at the voxel  $v$  is

$$\hat{\mu}_v^{\text{Sed}} = \frac{\vartheta}{b} \hat{\beta}_v^{\text{Sed}} \quad [\text{gr}], \quad (3.13)$$

and the total sediment cloud mass is

$$\hat{\mu}_{\text{total}}^{\text{Sed}} = \sum_v \hat{\mu}_v^{\text{Sed}} \quad [\text{gr}]. \quad (3.14)$$

### 3.3 SART

Common CT systems use techniques based on Radon and Fourier transforms to reconstruct the 3D distribution of matter in the observed volume. These techniques require a large number of uniformly spaced projections. The projections are usually acquired from a sensor rotating around a stationary target, as in medical CT. These methods are not suitable for reconstructing time-evolving heterogeneous media or use of non uniformly spaced projections. For dynamic fluids, simultaneous imaging from multiple and finite views is required. Algebraic approaches as the simultaneous algebraic reconstruction technique (SART) [61, 62] were previously used in particles and fluids studies [20, 21, 23], since they are suited for setups having limited views. These methods operate in the spatial domain, and involve grid volumes similar to  $\beta^{\text{Sed}}(\mathbf{X})$ , and solve discrete problems as presented in Eq. (3.9).

Define

$$\tilde{\mathbf{A}} \triangleq \begin{bmatrix} \mathbf{A} \\ \sqrt{\alpha} \mathcal{L} \end{bmatrix} \in \mathbb{R}_+^{(m+n) \times n}, \quad (3.15)$$

and

$$\tilde{\boldsymbol{\tau}} \triangleq \begin{bmatrix} \boldsymbol{\tau} \\ \mathbf{0} \end{bmatrix} \in \mathbb{R}_+^{(m+n) \times 1}. \quad (3.16)$$

Then using algebraic manipulations Eq. (3.9) can be rewritten in a compact manner

$$\hat{\boldsymbol{\beta}}^{\text{Sed}} = \arg \min_{\boldsymbol{\beta}^{\text{Sed}}} \left( \left\| \tilde{\mathbf{A}} \boldsymbol{\beta}^{\text{Sed}} - \tilde{\boldsymbol{\tau}} \right\|_2^2 \right) \quad \text{s.t. } \boldsymbol{\beta}^{\text{Sed}} \geq 0. \quad (3.17)$$

SART is a variant of a projected gradient descent method of solving linear problems. Let  $\mathcal{C}$  expresses non-negativity of the solution  $\boldsymbol{\beta}^{\text{Sed}}$ , i.e.,  $\mathcal{C} \in \mathbb{R}_+^{n \times 1}$ . Let the operator  $\mathcal{P}_{\mathcal{C}}$  to be a projection on the convex set of constraints  $\mathcal{C}$ . A matrix element of  $\tilde{\mathbf{A}}$  is denoted as  $\tilde{a}_{q,v}$ , having row and column indices,  $q \in 1..m + n$  and  $v \in 1..n$ , respectively. Let

$$\tilde{a}_q = \sum_v \tilde{a}_{q,v}, \quad (3.18)$$

and

$$\tilde{a}_v = \sum_q \tilde{a}_{q,v}, \quad (3.19)$$

to be the row and column sums of  $\tilde{\mathbf{A}}$ , respectively. Let draw the diagonal matrices

$$\mathbf{D}_{\text{row}} = \text{diag}(\tilde{a}_q), \quad (3.20)$$

and

$$\mathbf{D}_{\text{col}} = \text{diag}(\tilde{a}_v). \quad (3.21)$$

The matrices  $\mathbf{D}_{\text{row}}$  and  $\mathbf{D}_{\text{col}}$  are positive definite, and used for preconditioning of  $\tilde{\mathbf{A}}$ .

Then, the solution update in each iteration  $k$  is of the following form [63]

$$\beta_{k+1}^{\text{Sed}} \leftarrow \mathcal{P}_C \left[ \beta_k^{\text{Sed}} + \zeta_k \mathbf{D}_{\text{row}}^{-1} \tilde{\mathbf{A}}^\top \mathbf{D}_{\text{col}}^{-1} \left( \tilde{\boldsymbol{\tau}} - \tilde{\mathbf{A}} \beta_k^{\text{Sed}} \right) \right]. \quad (3.22)$$

Here,  $\zeta_k$  is the step size of each iteration  $k$ . Convergence of SART is guaranteed for  $0 \leq \zeta_k \leq 2$ .



# Chapter 4

## Design of the electro-optical tomography setup

This chapter describes the design of the electro-optical setup used in the tomography system. The chapter begins with the spatial and the temporal requirements of the setup, followed by imaging and engineering considerations of the components. Several imaging components were considered to be used in the system. The tomography concept is then examined in Chapter 5 for setups containing these components. This leads to the final configuration of the system used in our tomography experiments, described in Chapter 6.

### 4.1 System requirements

The imaging system resolution is determined by the camera, lens, and the working distance from the cloud. We derive the required spatiotemporal resolution from biological resuspension event characteristics and from observations made by marine researchers involved in this study. We define an *underwater observation volume* (UOV) containing a suspended particle cloud that the system will observe. The system is set to have a 1.5 [m] field of view (FoV) from a 3 [m] working distance, with spatial and temporal resolutions of 1 [cm<sup>3</sup>] and 1 [sec], respectively. To minimize flow disruptions, we set the working distance above the UOV, and place the horizontal lighting system underneath the UOV. For a uniform illumination, we chose to use a diffuse planar visible light source. The initial requirements are summarized in Table 4.1 and visualized in Fig. 4.1. Based on these requirements, this chapter outlines the optical considerations for selecting camera and lens types (Section 4.2), and the radiant power of the illumination system (Section 4.3).

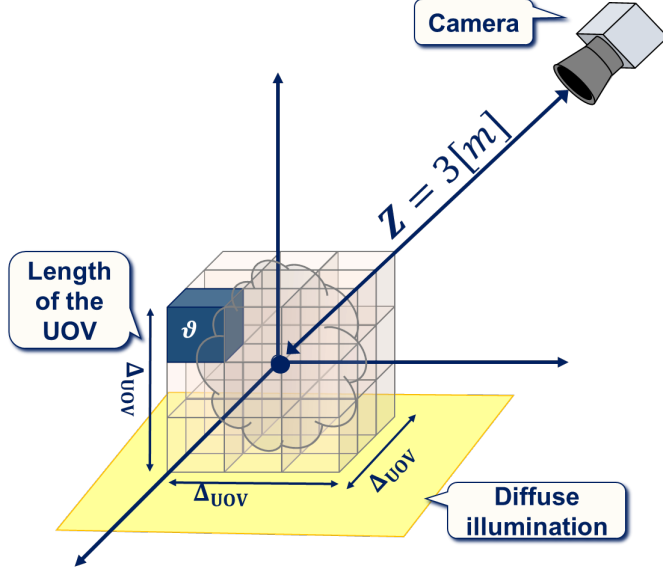


Fig. 4.1. Visualization of imaging requirements.

Property	Requirement
Z	3 [m]
$\Delta_{\text{UOV}}^3$	$1.5 \times 1.5 \times 1.5 [\text{m}^3]$
$\vartheta$	$1 \times 1 \times 1 [\text{cm}^3]$
fps	$1 [\text{sec}^{-1}]$

Table 4.1: Imaging requirements.

## 4.2 Imaging spatial resolution

The imaging system in Fig. 4.2 (right) has focal length  $f$  and lens aperture of diameter  $\Delta_{\text{lens}}$  is focused on a point on the focusing plane (left), at distance  $Z$  from the camera's lens. Using the imaging condition given by the thin lens equation,

$$\frac{1}{f} = \frac{1}{f_{\text{CCD}}} + \frac{1}{Z} \left[ \frac{1}{\text{mm}} \right], \quad (4.1)$$

the distance  $f_{\text{CCD}}$  of the sensor plane from the lens plane is extracted. Every point outside the focus plane is blurred on the sensor plane, appearing as if the point originated from a disk having diameter  $\Delta_{\text{object}}$  on the focus plane. The depth of field (DoF) of the camera defines a distance range in which all of the out-of-focus points can still be observed as if in focus. We define the forward and rear bounds of the required DoF by  $Z_f$  and  $Z_r$ , respectively. Using geometric similarity,

$$\Delta_{\text{object}} = \Delta_{\text{lens}} \frac{|Z_r - Z|}{Z_r} [\text{mm}]. \quad (4.2)$$

Here,

$$\Delta_{\text{lens}} = \frac{f}{f_{\#}} \quad [\text{mm}], \quad (4.3)$$

where  $f_{\#}$  is the f-number of the lens. The image defocus blur kernel is a circle of confusion (CoC) of diameter  $\Delta_{\text{sensor}}$ . It is related to  $\Delta_{\text{object}}$  by a magnification relation, extracted from the system's geometric similarity

$$\Delta_{\text{sensor}} = \frac{f_{\text{CCD}}}{Z} \Delta_{\text{object}} \quad [\text{mm}]. \quad (4.4)$$

As the projected diameter becomes large relative to pixel size  $\Delta_{\text{pix}}$ , the image sharpness degrades. Therefore,  $\Delta_{\text{pix}}$  is the CoC limitation on the sensor plane for points in the DoF. The lens resolution quantifies how imaged lines-pairs (lp) can be near one other, and still be visibly resolved. The modulation transfer function (MTF) is the lens response to a variety of spatial frequencies. The frequency is defined as  $[\frac{\text{lp}}{\text{mm}}]$ , and satisfies

$$\left[ \frac{\#\text{lp}}{\text{mm}} \right] = \frac{1}{\Delta_{\text{sensor}} \text{ [mm]}}. \quad (4.5)$$

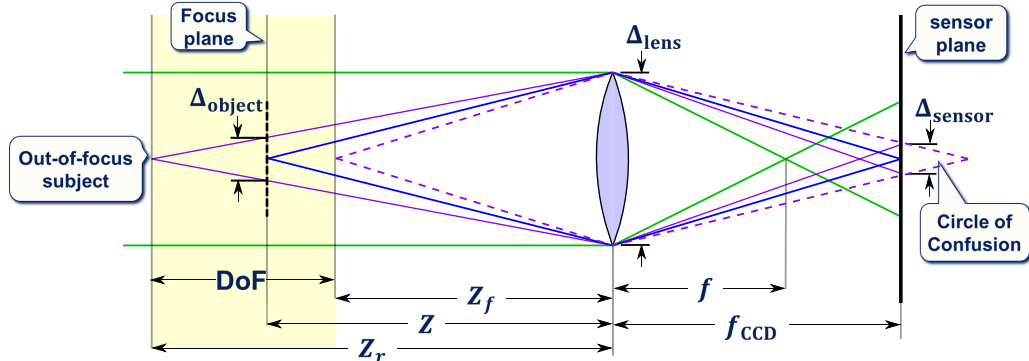


Fig. 4.2. Spatial resolution specifications of the imagine system.

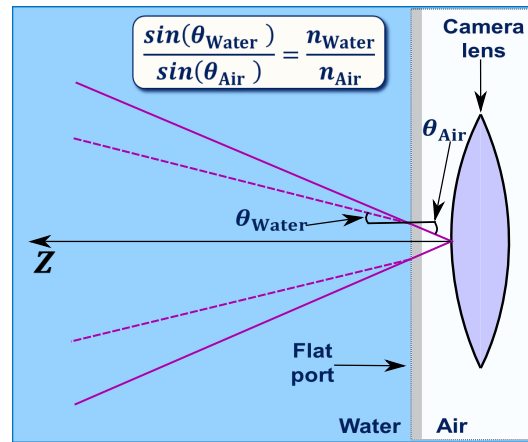


Fig. 4.3. Flat port and Snell's law.

When imaging a water medium from a sealed housing, the light is refracted by the flat port (Fig. 4.3) according to *Snell's law*. The refractive indices of water and air are  $n_{\text{Water}} = 1.33$  and  $n_{\text{Air}} = 1$ , respectively. Ray bending creates a virtual image of objects, appearing closer than if they were in air. When observing through a thin flat port, objects that are close to the optical  $Z$  axis, the effective optical length of the camera is extended [29] for magnifications calculations (not focus calculations),

$$f_{\text{effective}} \approx n_{\text{Water}} f \quad [\text{mm}]. \quad (4.6)$$

We now detail the resolution analysis for a setup containing an IDS UI3260xCP-C camera. This camera has  $\Delta_{\text{pix}} = 5.86 \text{ } [\mu\text{m}]$ . It is fitted here with a Tamron M112FM12 lens having  $f = 12 \text{ } [\text{mm}]$  and  $f_{\#} \in [2, 16]$ . Using Eqs.(4.1)–(4.6), the CoC of points at varying distances  $Z$ , are plotted in Fig. 4.4 for several values of  $f_{\#}$ . When  $f_{\#} \in [4, 16]$ , the CoC's are at most the size of  $\Delta_{\text{pix}}$  (blue dashed-line). Thus, points in the range of the UOV are likely to be visibly sharp. From Eq. (4.4), the circle of  $\Delta_{\text{object}} = 1 \text{ } [\text{cm}]$  diameter on the focus plane is projected to  $\Delta_{\text{sensor}} \approx 54 \text{ } [\mu\text{m}]$  on the sensor plane (orange dashed-line). This means that  $\sim 9$  pixels observe 1  $[\text{cm}]$  in the field. The spatial frequency corresponding to  $54 \text{ } [\mu\text{m}]$  is  $19 \text{ } [\frac{\text{lp}}{\text{mm}}]$ . In this frequency, Fig. 4.5 shows that the MTF is 90% (orange dashed-line). The above analysis shows that the optical resolution of this setup easily accommodates the requirement of 1  $[\text{cm}]$  resolution in the field. Several setups were analyzed this way and simulated (Chapter 5).

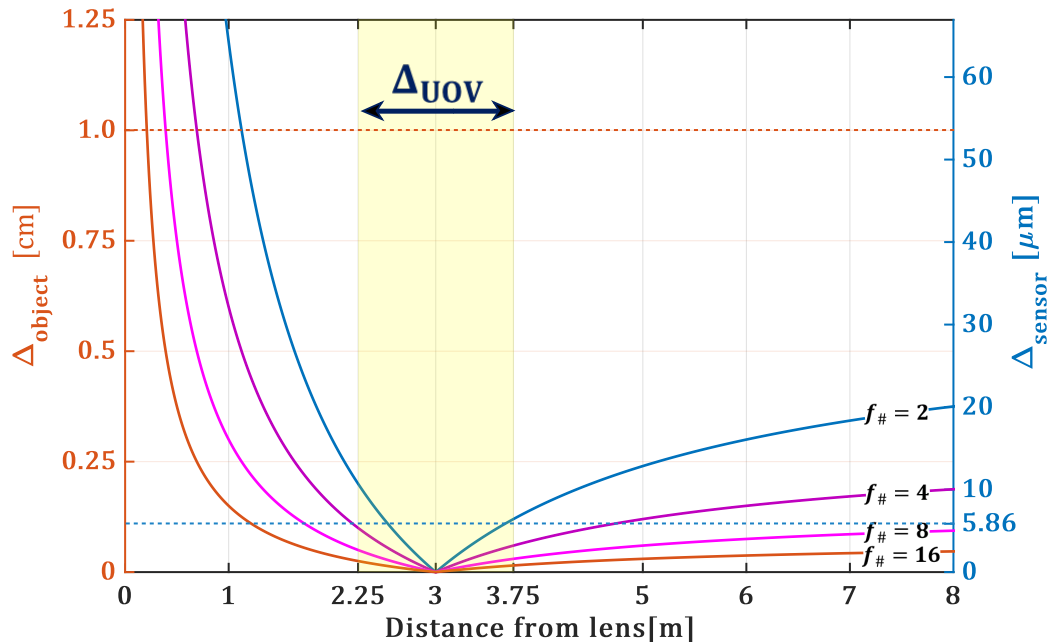


Fig. 4.4. Circle of confusion diameter as function of distance for an imaging system focused at  $Z = 3 \text{ [m]}$  in water, with focal length  $f = 12 \text{ [mm]}$  for several values of lens f-number  $f_{\#}$ .

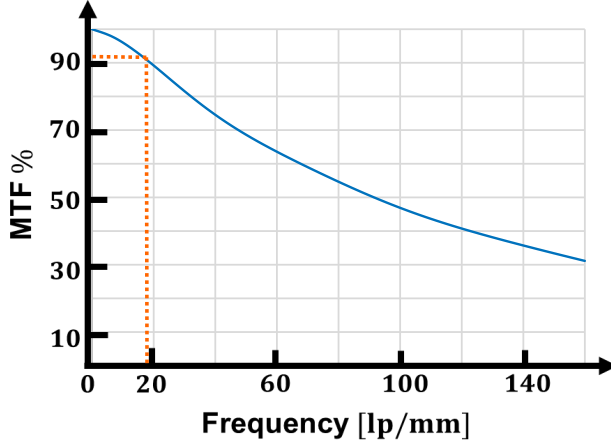


Fig. 4.5. Modulation Transfer Function (MTF) of a Tamron MTFM112F12, 12 [mm] lens [64]. The orange-dashed line yields MTF of 90% at  $19 \frac{\text{lp}}{\text{mm}}$ . This spatial frequency corresponds to a blurred circle with diameter  $\Delta_{\text{sensor}} \approx 54 \mu\text{m}$ .

### 4.3 Light screen intensity

We selected cameras and lenses that suit the resolution requirements. As we now show, this led to lighting intensity calculations. The calculations aim to achieve the minimum radiant power  $\mathcal{L}_{\text{screen}}$  [lm] by the screen while having maximum readout values by the cameras. A higher radiant power enables reduction of exposure time. The calculation is based on radiometric electronic considerations for estimating pixel energy in Joules,  $J_p^{\text{rad}}$  and  $J_p^e$  respectively.

The scene shown in Fig. 4.6 includes a diffuse lighting screen (left) in parallel to the camera sensor plane (right). The radiance  $i_p^{(0)}$  emitted from a small region on the screen corresponds to pixel  $p$  on the camera sensor plane. For a diffuse screen, the emitted radiant exitance is achieved by integrating  $i_p^{(0)}$  over a hemisphere

$$M = \int_{\Omega \in 2\pi} i_p^{(0)} d\omega = 2\pi i_p^{(0)} \left[ \frac{\text{W}}{\text{m}^2} \right], \quad (4.7)$$

where  $\omega \in \mathbb{S}^2$  is a solid angle on the screen plane. Let  $i_p$ , be the corresponding incoming scene radiance, arriving at angle  $\theta^{\text{Water}}$  to the camera housing. As presented in Section 3.1,  $i_p$  is modeled according to the Beer-Lambert law. Recall that we seek a maximum camera readout value. The maximum energy of pixel  $p$  is obtained when imaging sediment-free water. Then by setting  $i_p^{\text{Ambient}} = 0$  in Eq. (3.1), and plugging Eq. (4.7),  $i_p$  becomes

$$i_p = \frac{M}{2\pi} \exp \left[ -\beta^{\text{Water}} \frac{Z}{\cos(\theta^{\text{Water}})} \right] \left[ \frac{\text{W}}{\text{m}^2 \text{sr}} \right]. \quad (4.8)$$

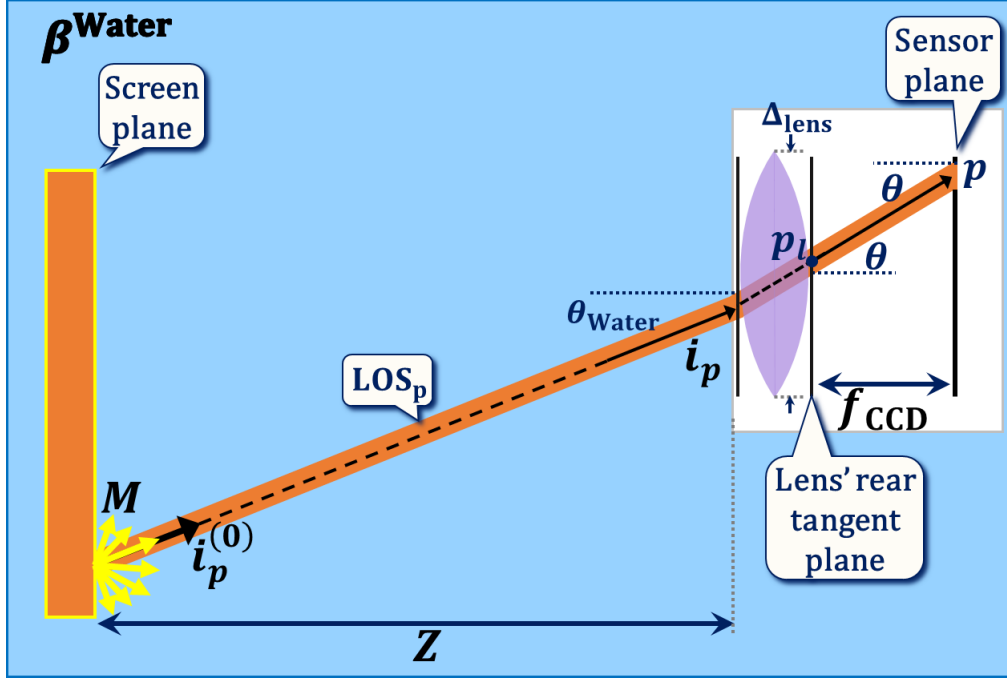


Fig. 4.6. The radiance excitation of screen

Let pixel  $p$  have a surface area of  $S_p = \Delta_{\text{pix}}^2$ . The camera lens is thin with diameter  $\Delta_{\text{lens}}$ , at distance  $f_{\text{CCD}}$  from the sensor plane. The incoming scene radiance  $i_p$  reaches the lens at angle  $\theta$ , and yields irradiance on the sensor plane around pixel  $p$  [65, 66]

$$E_p = \frac{i_p \pi \cos^4(\theta)}{4} \left( \frac{\Delta_{\text{lens}}}{f_{\text{CCD}}} \right)^2 \left[ \frac{W}{m^2} \right]. \quad (4.9)$$

Integrating  $E_p$  over pixel area  $S_p$  and over exposure time  $t_{\text{exp}}$  yields the energy measured at  $p$

$$J_p^{\text{rad}} = \int_{t_{\text{exp}}} \int_{S_p} E_p dS_p dt = E_p \Delta_{\text{pix}}^2 t_{\text{exp}} \quad [\text{Joules}]. \quad (4.10)$$

The maximum pixel energy is achieved for the lowest angle within the system FoV. Thus, by setting  $\theta^{\text{Water}} = \theta = 0$ , and plugging Eqs. (4.8) and (4.9), the pixel energy becomes

$$J_p^{\text{rad}} = \frac{M \Delta_{\text{pix}}^2 t_{\text{exp}}}{8} \exp[-\beta^{\text{Water}} Z] \left( \frac{\Delta_{\text{lens}}}{f_{\text{CCD}}} \right)^2 \quad [\text{Joules}]. \quad (4.11)$$

The light energy of a pixel can also be expressed using electronic consideration. Each photon's energy is

$$J_{\text{photon}}^\lambda = \frac{hc}{\lambda} \quad [\text{Joules}], \quad (4.12)$$

where  $h$  is Planck constant and  $c$  is the speed of light. The probability of an electron generated per incident photon is given by the quantum efficiency (QE) of the sensor response to arriving photons at wavelength  $\lambda$ , noted as  $\text{QE}^\lambda$ . When the pixel is saturated,

it holds the  $N_{\text{well}}$  electrons. Then the number of photons generating electrons is

$$N_{\text{photons}}^{\lambda} = \frac{N_{\text{well}}}{\text{QE}^{\lambda}} \quad [\text{e}^-], \quad (4.13)$$

Then using Eqs. (4.12) and (4.13), meeting the condition of near-saturated camera pixel, light energy incident on camera pixel  $p$  is

$$J_p^e = N_{\text{photons}}^{\lambda} J_{\text{photon}}^{\lambda} \quad [\text{Joules}]. \quad (4.14)$$

Deriving the required screen radiant exitance  $M$ , is done by equating Eq. (4.11) ( $J_p^{\text{rad}}$ ) to Eq. (4.14) ( $J_p^e$ ), and plugging Eqs. (4.1) and (4.3)

$$M = \frac{8N_{\text{Well}}J_{\text{photon}}^{\lambda}}{\Delta_{\text{pix}}^2 t_{\text{exp}} \text{QE}^{\lambda}} \left( f_{\#} \frac{Z}{Z-f} \right)^2 \exp[\beta^{\text{Water}} Z] \quad \left[ \frac{\text{W}}{\text{m}^2} \right] \quad (4.15)$$

Let the screen have a surface area  $S_{\text{screen}}$ , and a diffusing layer with transmission efficiency of  $T_{\text{diffuser}}$ . Then the total radiant power of the screen is

$$\Phi_{\text{screen}} = \frac{MS_{\text{screen}}}{T_{\text{diffuser}}} \quad [\text{W}]. \quad (4.16)$$

The radiant power is converted to lumen units

$$\mathcal{L}_{\text{screen}} = \kappa \Phi_{\text{screen}} \quad [\text{lm}], \quad (4.17)$$

where  $\kappa = 588.746 \left[ \frac{\text{W}}{\text{lm}} \right]$  is the photopic conversion value of corresponding to  $\lambda = 529 \text{ [nm]}$  [67]. The calculation of  $\Phi_{\text{screen}}$  is done for the imaging set presented in Section 4.2. We base the calculation on a green wavelength since

1. In our range of  $Z$ , the green light is less attenuated.
2. The emission spectrum of a typical white LED is very efficient in the green wavelengths.
3. The number of green pixels is twice the number of red or blue pixels in the sensor, having an RGGB Bayer pattern.
4. The sensor is more efficient in this wavelength.
5. The human eye is more sensitive to green light.

The values used in the calculation were:  $Z = 3 \text{ [m]}$ ,  $S_{\text{screen}} = 1 \text{ [m}^2]$ ,  $T_{\text{diffuser}} = 0.7$ . According to the camera specifications [68]  $N_{\text{Well}} = 32870 \text{ [e}^-]$ ,  $\text{QE}^{\lambda} = 70\%$  (Fig. 4.7). We set  $f_{\#} = 8$ , which is in the range shown in Fig. 4.4. We used the extinction coefficient corresponding to the green channel to be  $\beta_{\text{green}}^{\text{Water}} = 0.16 \left[ \frac{1}{\text{m}} \right]$ . For  $t_{\text{exp}} \in [10, 20] \text{ [msec]}$ , the estimated radiant power of the screen is  $\mathcal{L}_{\text{screen}} \in [18, 36] \text{ [Klm]}$ . Based on this calculation we constructed the screen described in Chapter 6.

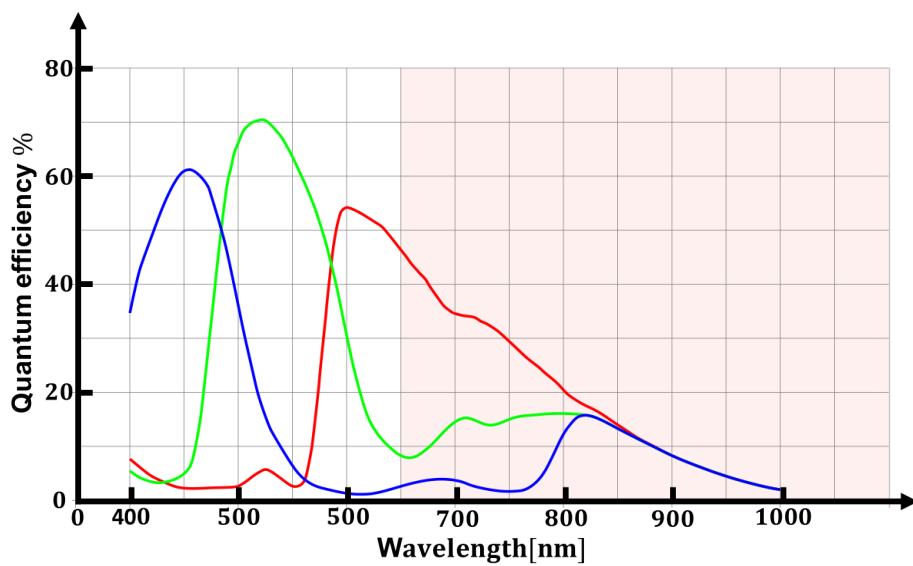


Fig. 4.7. Quantum Efficiency  $\text{QE}^\lambda$  graphs of an IDS UI3260xCP-C camera [68]. The line colors correspond to RGB channels, and the red background area corresponds an IR-blocking filter.

# Chapter 5

## Simulations

We tested the tomography concept using both lab experiments and simulations. The simulation environment contained an underwater 3D scene, a submerged diffuse illuminating screen, machine vision cameras and a 3D sediment cloud. Using radiation transfer solver [65, 69], we synthesized the observed underwater images. Then, we performed 3D tomographic reconstruction. The simulated ground truth helped design the imaging configuration by considering how camera specifications (type, amount and poses) affect the reconstruction quality.

### 5.1 Renderings

During simulations we set  $i_p^{\text{Ambient}} = 0$ . The volumetric domain has  $n = 128 \times 50 \times 128$  voxels. Similarly to [25, 27, 59], the radiative transfer simulations relied on volumetric optical parameters, which are the extinction coefficient  $\beta(\mathbf{X})$ , single scattering albedo  $\varpi(\mathbf{X})$  and anisotropy parameter  $g_{\text{HG}}$  of a Henyey-Greenstein scattering phase function. We specifically used typical clear ocean water optical properties [70, 71]. In these waters, corresponding to RGB channels,  $\beta^{\text{Water}} \triangleq (0.583, 0.16, 0.15) [\text{m}^{-1}]$ ,  $\varpi(\mathbf{X}) \triangleq (0.228, 0.625, 0.667)$ , and  $g_{\text{HG}}^{\text{Water}} \triangleq 0.9$ . The sediment extinction coefficient  $\beta^{\text{Sed}}(\mathbf{X})$  is spatially heterogeneous and spectrally uniform. As a proxy for a sediment cloud, we used an open source *smoke* phantom [69]. We aimed to simulate a dense sediment cloud for which on average  $\langle \beta(\mathbf{X}) \rangle_{\mathbf{X}} = 3.3 [\text{m}^{-1}]$ , corresponding to a 30[cm] visibility range. Thus we scaled the phantom's range of extinction coefficients to  $\beta(\mathbf{X}) \in [0, 12.2] [\text{m}^{-1}]$ . In the simulations, we set  $\varpi^{\text{Sed}}(\mathbf{X}) = 0$ .

The imaging sensor follows a perspective camera model, with a set field of view, image resolution, and Bayer pattern. These parameters are set by the specifications of an off-the-shelf machine vision camera, e.g., IDS UI3260xCP-C. In particular these specifications enabled us to render realistic noise in the simulated images. Let  $\nu_e^P$  be the photon signal generated by Monte-Carlo simulations of light propagation. The maximum photon signal  $\nu_e^P$  generates  $N_{\text{well}} [\text{e}^-]$  photo-electrons in a saturated pixel. Let  $\gamma_e [\text{e}^-]$  to be the number of photo-electrons per camera gray level. To induce noise

we took the following steps:

1. An effect similar to photon noise is induced by introducing zero-mean Gaussian noise which has a variance equal to  $\nu_e^P [e^-]$ .
2. To emulate readout noise, zero-mean Gaussian noise with fixed variance  $\sigma_{\text{read\_e}} [e^-]$  is added. Thus pixel intensity of a noisy image is  $i_e \sim \mathcal{N}(\nu_e^P, \nu_e^P + \sigma_{\text{read\_e}}^2) [e^-]$ .
3. We introduced quantization noise by converting photo-electrons counts to gray levels using  $i_p = \lfloor i_e / \gamma_e \rfloor \in \mathbb{N}$ .

For example, for the IDS UI3260xCP-C camera, the applied specifications [68]:  $N_{\text{well}} = 32870 [e^-]$ ,  $\sigma_{\text{read\_e}} = 6.2 [e^-]$ ,  $\gamma_e \approx 128.4 [e^-]$ . The renderings were performed on a machine of type M4.16Xlarge, of the Amazon Elastic Computing Cloud [72].

## 5.2 Simulated tomographic reconstructions

Based on camera poses and sediment phantom position, we calculated a sparse projection matrix  $\mathbf{A} \in \mathbb{R}^{m \times n}$  using ray tracing [73]. We used the *AIRtools* implementation [63] of the Simultaneous Algebraic Reconstruction Technique (SART) [61]. Reconstruction quality compares the estimated  $\hat{\beta}^{\text{Sed}}$  to the original phantom  $\beta^{\text{Sed}}$ , in terms of unitless global [25] and local [26] measures

$$\delta = \frac{\|\hat{\beta}^{\text{Sed}}\|_1 - \|\beta^{\text{Sed}}\|_1}{\|\beta^{\text{Sed}}\|_1}, \quad (5.1)$$

$$\epsilon_2 = \frac{\sqrt{\frac{1}{n} \|\hat{\beta}^{\text{Sed}} - \beta^{\text{Sed}}\|_2^2}}{\max(\beta^{\text{Sed}})}. \quad (5.2)$$

Here we describe representative results for the simulations process of the scenario illustrated in Fig. 5.1(a). The cameras are uniformly spaced on a  $125^\circ$  horizontal arch at height 0.5[m], facing the cloud from a 3[m] distance. The phantom is of size  $1 \times 0.39 \times 1 [m^3]$  having voxel resolution of 0.78[cm], and the camera type is IDS UI3260xCP-C. Each column in Fig. 5.1(b) shows rendered images and optical depths for three different views. The reconstructed volumetric extinction coefficient of the cloud retrieved from eight cameras is presented at Fig. 5.1(c). The reconstruction error  $\epsilon_2$  as a function of the number of cameras is presented in Fig. 5.1(d). We received similar results for other camera types and positions. The local error  $\epsilon_2$  dropped as the number of cameras increased. The global error  $\delta$  saturated at  $\delta = 0.08$ .

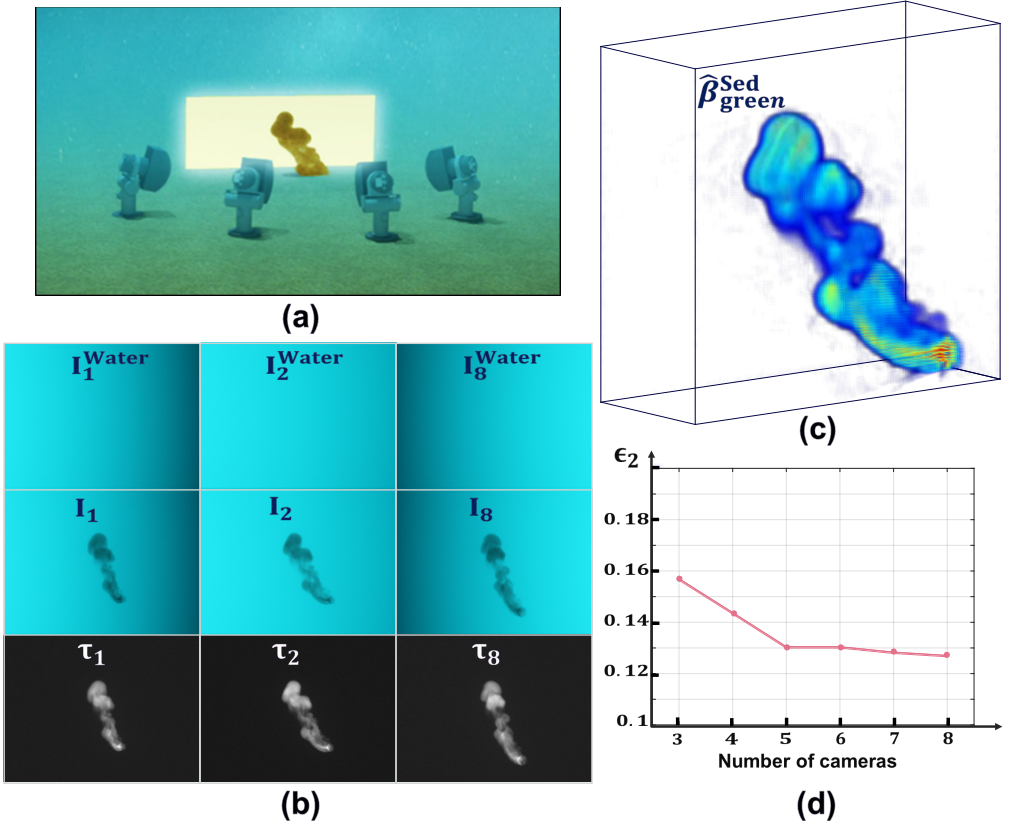


Fig. 5.1. Simulations. (a) Scenario illustration: the cameras are distributed uniformly on a  $125^\circ$  arch of height of  $0.5$  [m], and facing the cloud from a  $3$  [m] distance. (b) Representative images of several side views (water images  $I^{\text{Water}}$ , cloud images  $I$ , optical depth images  $\tau$  in the green channel). (c) The reconstructed  $\hat{\beta}^{\text{Sed}}$  of the cloud . (d) Reconstruction errors vs. the number of IDS UI3260xCamera-C cameras.



# Chapter 6

## Tomographic experiments

### 6.1 System and method

We performed experiments in the research seawater pool of dimensions  $6 \times 3 \times 3$  [ $\text{m}^3$ ], at The Leon H. Charney School of Marine Sciences, University of Haifa, Israel. Inspired by the *communicating vessels* principle, we built an injection system, illustrated in Fig. 6.1(a), connected at its top to a 10 [ $\text{L}$ ] *source tank*. The source tank contained MP SILICA particles suspended in water. The particle size range is 12–26 [ $\mu\text{m}$ ]. This range suits in the particle sizes of silt, clay, and fine sand, which exist along the Israeli Mediterranean shelf [74], at sites deeper than 30 [ $\text{m}$ ]. The source tank was partially drained, creating a resuspended cloud emanating from the middle of the lighting screen.

The optical system contained eight machine vision cameras having a linear radiometric response. We used IDS UI3260xCP-C cameras with Tamron M112FM12 12 [ $\text{mm}$ ] lenses, sealed inside designated housings having flat ports (windows), as shown in Fig. 6.1(b). According to [29], when a perspective camera resides in an air chamber having a flat port and is embedded in a water medium, refraction causes the imaging system to have a non-single viewpoint. Nonetheless, it is possible to approximate these systems as having a single view point [29] by setting a tight lens–port distance.<sup>1</sup> In such conditions, refractions induce two-dimensional image distortions, which can be accommodated digitally using camera calibration. Therefore, each camera was placed inside the housing while keeping the port relatively tangent to the lens. The cameras are mounted on a frame above a lighting screen, Fig. 6.2(a). Each camera was directed to the volume of interest and set to have  $\sim 2.7$  [ $\text{m}$ ] working distance from the middle of the screen. The illumination screen is composed of sealed LEDs mounted between two diffuse white PVC boards, emitting a total of 24000 [ $\text{lm}$ ], Fig. 6.2.

We used a calibration board, markers on the screen as in Fig. 6.2(c), *openCV* [75], and *Agisoft* software [76] to calibrate the system geometry. This led to the sparse projection matrix  $\mathbf{A}$  used in Eqs. (3.8) and (3.9). Before each resuspension event, we

---

<sup>1</sup>Dome-ports can mitigate refraction distortions if the dome center aligns with the lens' center of projection.

imaged the lighting screen when active and not active, to acquire measurements of  $i_p^{\text{Water}}$  and  $i_p^{\text{Ambient}}$  respectively. Throughout each event, we imaged the evolving cloud to acquire measurements of  $i_p$ , at 10 frames per second.

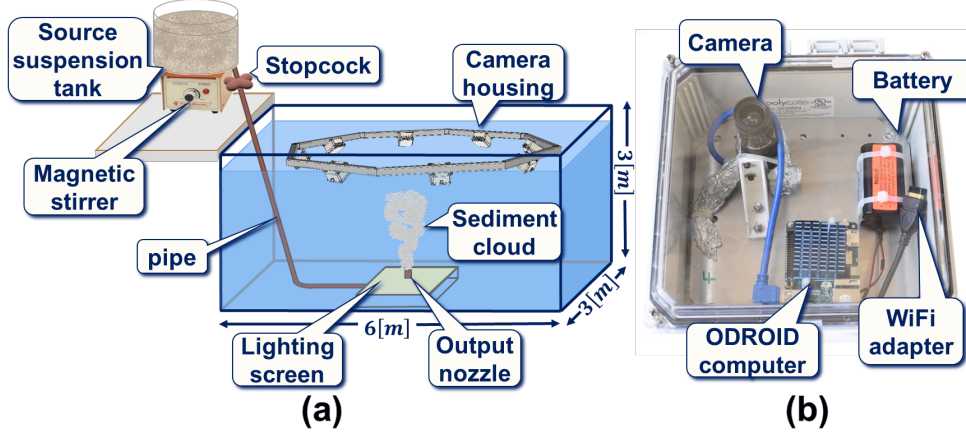


Fig. 6.1. (a) System design. (b) The camera housing is made of polycarbonate resin, and contains: an ODROID XU-4 computer, an IDS UI3260xCP-C camera with Tamron M112FM12 12[mm] lens, Li-ion batteries and a nano USB WiFi adapter.

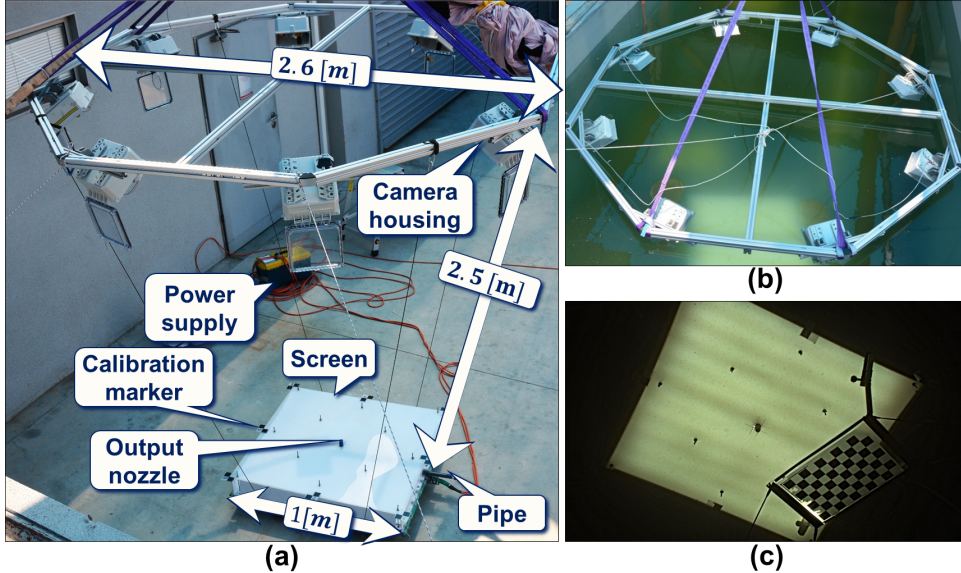


Fig. 6.2. (a) Side view of the system outside of the pool. The nozzle emerges from the middle of the screen, and camera's rig is centered above the screen at height of 2.5[m]. (b) Top view of the system submerged in a seawater pool. (c) Submerged screen and active calibration board.

## 6.2 Tomography reconstructions

Using Eq. (3.6), we retrieved the optical depths  $\{\tau_p\}_{p=1}^m$  of the suspended sediment cloud through time. Representative images are shown in Fig. 6.3(a). We performed reconstruction similarly to Section 5.2. The following steps, as shown in Fig. 6.3, improved the quality and runtime: (a) Pruning pixels by segmenting [77] and cropping

of the normalized optical depth images. (b) Reconstructing an initial solution  $\hat{\beta}^{\text{Sed}(0)}$ , using the un-pruned pixels, and  $\alpha = 0$ . Then, deriving the visual hull [78] of  $\hat{\beta}^{\text{Sed}(0)}$ . (c) Reconstructing  $\hat{\beta}^{\text{Sed}}$  within the visual hull, using  $\alpha = 0.45$ . The 3D results in Fig. 6.3 are for the green channel in a 2 [cm] voxel resolution, thus having voxel volume  $\vartheta = 8 \text{ [cm}^3]$ .

Using an independent lab experiment, we calibrated the coefficient  $b$  which relates  $\beta_v^{\text{Sed}}$  to  $\rho_v^{\text{Mass}}$  in Eq. (3.12). This experiment is described in Section 6.3. Then using Eqs. (3.12)–(3.14) we calculated the sediment cloud mass density  $\hat{\rho}^{\text{Mass}}$  and mass  $\hat{\mu}^{\text{Sed}}$ . This yielded an estimate of the evolving sediment cloud mass. We compared sediment mass estimation between two different experiments, each having different density in the source tank: 22.5 [ $\frac{\text{mgr}}{\text{cm}^3}$ ], and 30 [ $\frac{\text{mgr}}{\text{cm}^3}$ ]. The estimated mass of the clouds through 5.5 [sec] from the cloud's initiation is plotted in Fig. 6.4(a). Each curve averages two experiment repetitions. Values in corresponding times are scatter-plotted in Fig. 6.4(b). The linear fit is consistent with the source densities ratio 30:22.5 = 1.33.

Ultimately as in any active system, the system size limits the measurement domain. We noticed that 5.5 [sec] after the cloud's initiation, the cloud expanded beyond the screen area. This leads erroneously to negative value of  $\tau_p$ , when using naively Eq. (3.6), beyond screen borders. These pixels were pruned in our algorithm. This phenomenon is emphasized using a figure which represents  $\tau_p$  using a false-color palette; Fig. 6.5 shows  $\tau_p$  in the optical green channel, 46 [sec] after the cloud's initiation.

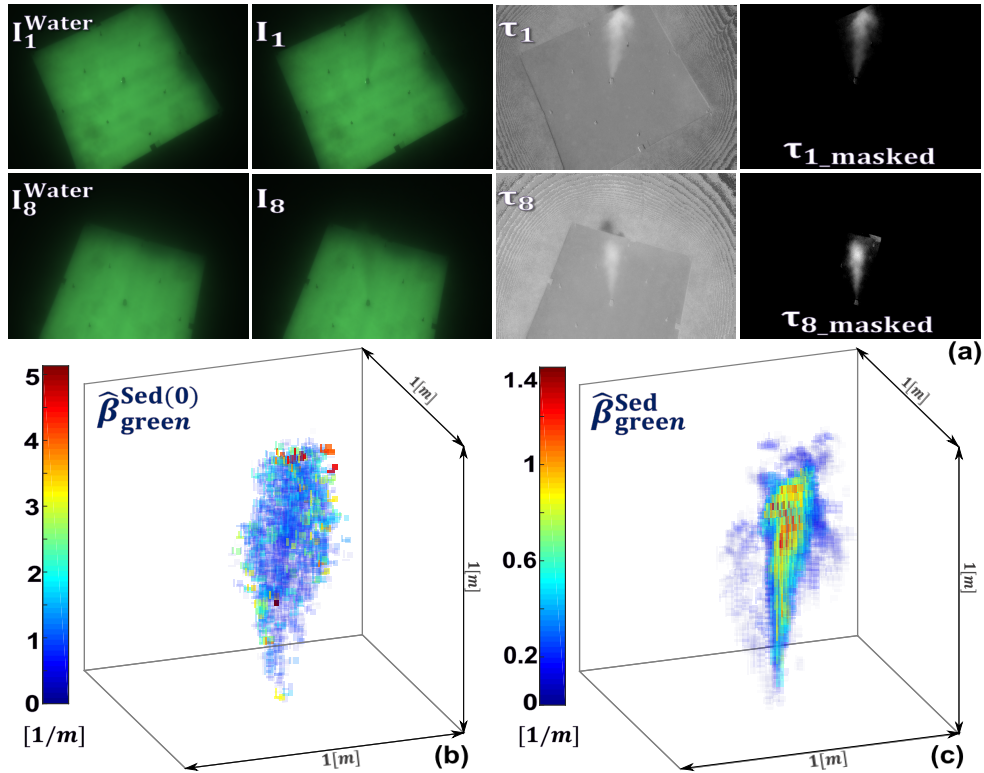


Fig. 6.3. Experiment: (a) Representative images of two cameras. Each camera yields a clear water image  $I^{\text{Water}}$ , an image having resuspension  $I$ ; The optical depth  $\tau$  in the green channel; A pruned optical depth image  $\tau_{\text{masked}}$ . (b) Initial reconstruction of the cloud  $\hat{\beta}^{\text{Sed}(0)}$  in the green channel. (c) Final reconstruction of the cloud  $\hat{\beta}^{\text{Sed}}$ .

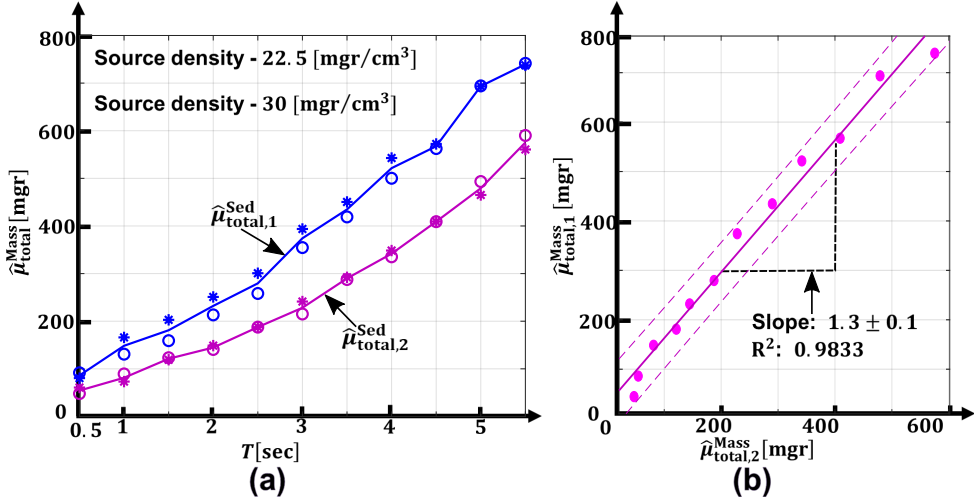


Fig. 6.4. (a) The estimated mass of a resuspension event, after each resuspension initiation. Each curve averages two experiment repetitions (shown as \* and ○). (b) Average reconstructed mass of  $30 \left[ \frac{\text{mgr}}{\text{cm}^3} \right]$  source suspension density ( $\triangleq \hat{\mu}_{\text{total},1}^{\text{Sed}}$ ) vs. average reconstructed mass of  $22.5 \left[ \frac{\text{mgr}}{\text{cm}^3} \right]$  source suspension density ( $\triangleq \hat{\mu}_{\text{total},2}^{\text{Sed}}$ ).

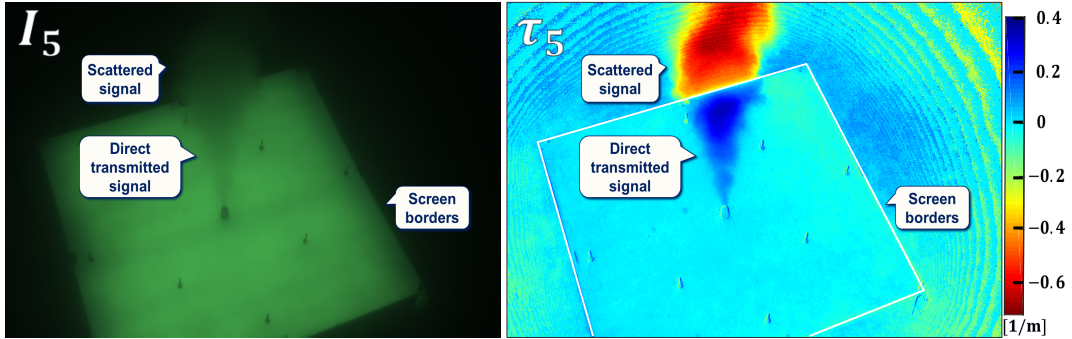


Fig. 6.5. (a) An RGB image of the cloud, 46 [sec] after the cloud's initiation. (b) The estimated optical depth  $\tau$  in the green channel. The values of  $\tau$  are presented in a false-color palette manner. Negative values beyond screen borders are due to scattered light contributing to measured radiance.

### 6.3 Sediment density calibration

Sediment density vs. extinction calibration was done in a small water tank, in a dark room, see Fig. 6.6. A glassware beaker is fixed above a stirring device inside the tank. The beaker contains a suspension of particles in 1 [L] water. A magnet stirring stick is used to maintain a uniform suspension. We used the imaging sensor described in Section 6.1. The lighting array includes: White LED (1 [W], 6500 [K], OPA733WD, Optek Technology), resistor of  $47\Omega$ , power supply of 3.335 [V] (Horizon Electronics DHR), DVM (34401A Digital Multimeter), optical mirror, and shutters.

The camera sampled the intensity of the light passing through the beaker. We first took a clear water image  $I^{\text{Water}}$ . Following this, we gradually added to the water beaker particles of roughly constant doses, until a final weight of 600 [mgr]. Here too, we

used MP SILICA of size range  $12 - 26 [\mu\text{m}]$ . For each session, we averaged intensity inside a rectangle measuring-area of  $10 \times 10$  pixels in the center of the beam and of the imaging sensor, over a second. Denote by  $i_{\text{rec}}^{\text{Water}}$ ,  $i_{\text{rec}}$  measurements of clear water and suspension, respectively, similarly to Eqs. (3.1) and (3.4). As the density of suspension increases, image intensity drops. Thus, during use of higher suspension concentrations we used longer exposures, then normalized the measurements accordingly.

From measurements of  $i_{\text{rec}}^{\text{Water}}$  and  $i_{\text{rec}}$ , and Eqs. (3.1) and (3.4) the retrieved extinction coefficient is

$$\beta^{\text{Sed}} = \frac{1}{l} \cdot \ln \left( \frac{i_{\text{rec}}^{\text{Water}}}{i_{\text{rec}}} \right), \quad (6.1)$$

where  $l = 0.092 [\text{m}]$  is the inner diameter of the beaker. A linear relation is extracted between the weight of particles in a volume of  $10^{-3} [\text{m}^3]$  water to the measured extinction coefficient  $\beta^{\text{Sed}}$  of the suspension, Fig. 6.7. Following [79] a linear fit should rely only on low concentrations for which multiple scattering is negligible. We included only measurements within the range of linear response. From the linear fit shown in Fig. 6.7, the estimated relation corresponding to RGB channels and used in Eq. (3.12) is  $b \approx (9.9, 9.6, 9.4) \cdot 10^{-3} [\frac{\text{m}^2}{\text{gr}}]$ .

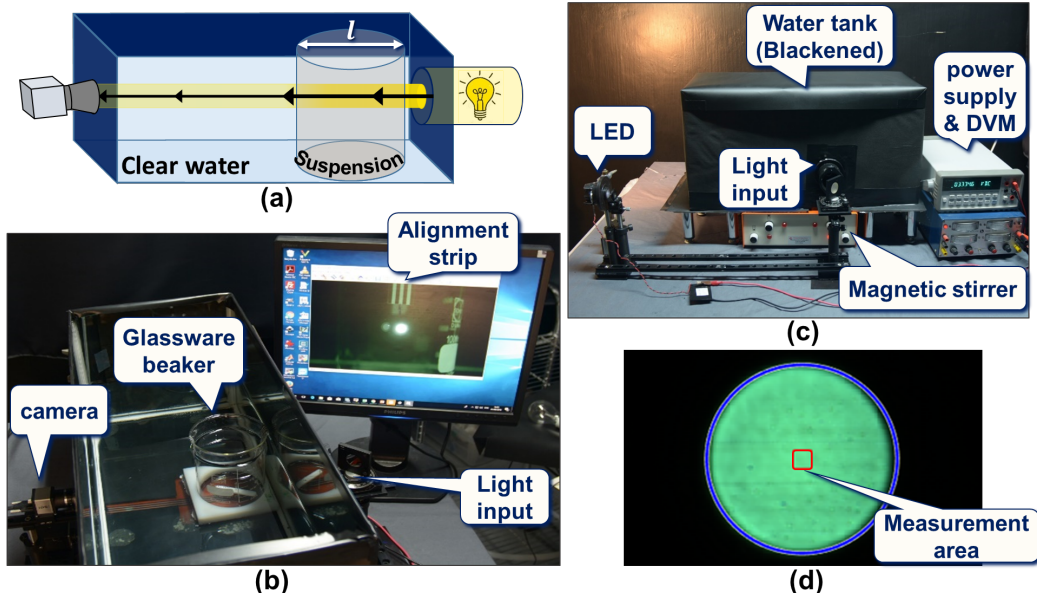


Fig. 6.6. Sediment calibration system. (a) Light path in a water tank from entry aperture through a glass beaker with particles suspension to camera side. (b) Top-side view. (c) Front view. (d) Water image  $I^{\text{Water}}$ .

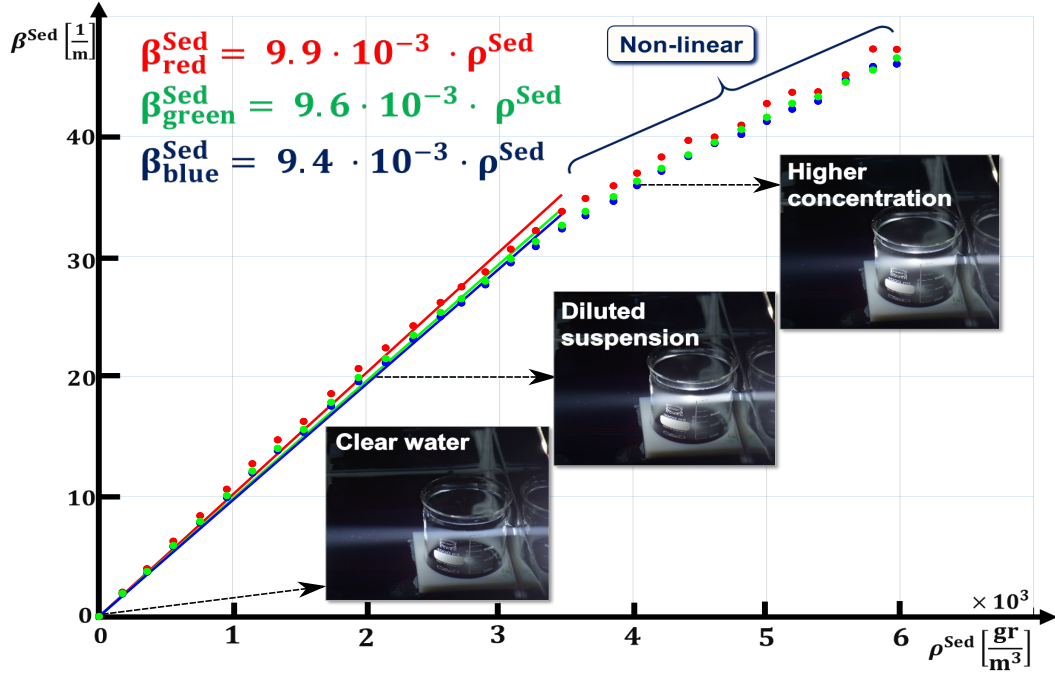


Fig. 6.7. Calibration results of  $\beta^{\text{Sed}}$  vs.  $\rho^{\text{Sed}}$  for RGB channels. The non-linear domain is due to multiple-scattering [79]. The images demonstrate the intensity attenuation of the transmitted light beam, for increasing particles density.

## 6.4 Injection system validation

To validate the consistency of the injection system, we performed repeatability tests. We assembled the injection system outside of the pool and prepared a suspension with a known density of  $5 \left[ \frac{\text{mgr}}{\text{cm}^3} \right]$  inside the source tank, Fig. 6.8(a). Then, we drained the suspension through the system into six containers. We repeated the process twice. We drained each container separately into a Büchner filter, Fig. 6.8(b). Then each paper filter was dried out and weighted. Using this process we retrieved in a single container particles mass density of  $4.0 \pm 0.5 \left[ \frac{\text{mgr}}{\text{cm}^3} \right]$ . The retrieval is approximately 81% of the particles that were originally put into the source tank. This percentage was consistent throughout twelve measurements thus giving confidence in the system's consistency. The loss of sediment could stem either from leftover that stayed within the injection system or from losses induced by filling and draining of containers during the validation process.

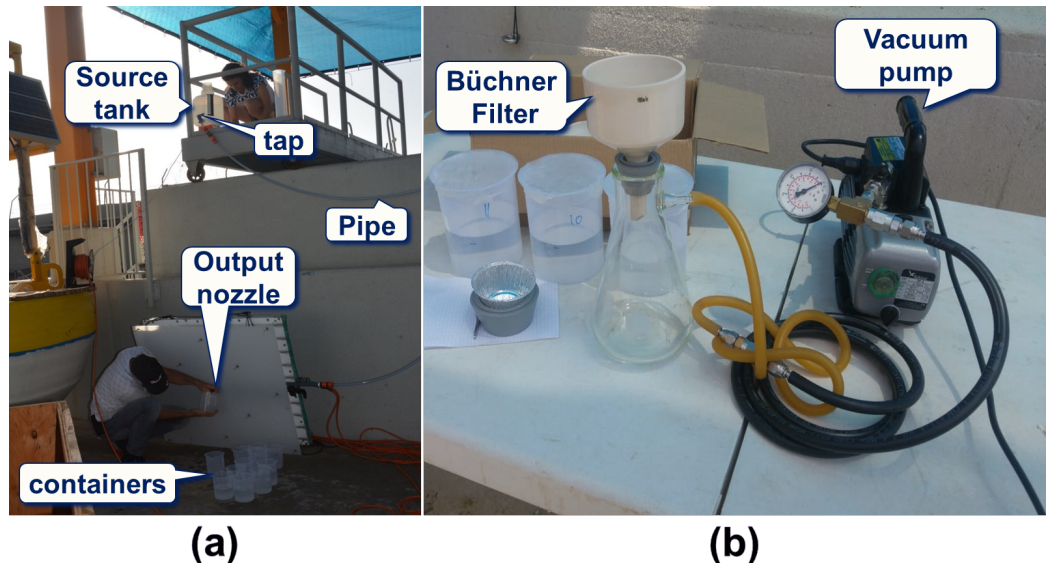


Fig. 6.8. Injection system validation. (a) Draining the suspension through the system into validation containers. (b) Filtering each container using Büchner filter.



# Chapter 7

## Discussion and outlook

This thesis proposes an approach for sensing and estimating the spatiotemporal distribution of underwater sediment resuspension. The solution adapts optical computed tomography principles to a multi-meter-scale underwater domain. The solution gives another dimensionality of sensing and expands the field of view of existing oceanographic in-situ methods. Existing in-situ approaches for quantifying sediment resuspension are very localized or focus on small scaled domains, 2D narrow sheets or 1D profiles. Our approach yields the 3D volumetric dynamic distribution of the suspension. The thesis goes beyond proposal of the concept, to include a theoretical formulation, computer simulations, engineering of a distributed optical imaging system, algorithm and eventual empirical validation.

The system design required incorporation of several aspects, including optical resolution, light refractions, radiometry, power, structuring of cameras' rig and lighting screen. The radiant capabilities of the screen allowed the adopting of an active calibration method, which benefited the calibration method and helped to achieve a better mapping of the 3D scene. Applying the *communicating vessels* principle enabled both the construction of the injection system and the observation of meter-scale sediment resuspension. Furthermore, creating a sediment calibration system, provided the weight estimation of the resuspended sediment cloud.

We performed several successful tomography experiments. The ability to schedule and control the tomography system, while performing experiments systematically enabled: Synchronizing images captured in all cameras for any time; And performing reconstructions over time and for varying sediment densities. Pruning pixels and applying the algorithm on to the screen's area and the bounding volume of the cloud (as in Fig. 6.5) simplified the retrieval model and improved both the quality and runtime of reconstructions. The speedup of the process allowed investigating repeatable resuspension events. The consistency between actual and expected results indicates the feasibility of our approach. It is thus possible to reconstruct underwater sediment cloud mass and dynamics in a meter-scale.

The algorithm we used assumes the resuspended cloud is diluted enough to suit the

single-scattering approximation. In a dense and wide cloud, this approximation may bias results. In the calibration described in Fig. 6.7, when reaching higher sediment densities the relation between optical density and particle density becomes non-linear. Therefore, for optical thickness satisfying  $\varpi^{\text{Sed}} \beta l > 1$ , we expect biased results. We believe that this bias can be largely mitigated using full 3D radiative transfer scattering tomography as in [25, 59, 80]. While this requires complex reconstruction algorithms [59, 80], the imaging system would still be similar to ours.

The thesis opens the door for quantitative in-situ research of marine sedimentation. We envision future developments for enabling field work in deep natural waters, which strive to minimize disturbance to nature. Future advancement may obviate active lighting in tomographic setups, for example relying on scatter of natural light [60], or by flipping the system. This also opens questions and leads to new challenges, such as introducing water surface caustics or other artificial light patterns to the image model. The significant off-scattered signal, as shown in Fig. 6.5, is yet to be exploited. Scattering can be considered as an information source, not only as a cause of extinction of light. Introducing other light components to the reconstruction model may be achieved by incorporating our approach in conjunction with turbidity sensors. Another possible improvement of our method is to integrate tools used in Neural Networks, by creating an automatic framework to generate smarter pixel masking through time. This will allow a faster and better reconstruction through time. Finally, the optical layout that we present, can be used in other applications. For example, it opens possibilities for inspecting other underwater phenomena such as the emergence of gas, oils, or other liquids.

# Bibliography

- [1] J. R. Valeur, A. Jensen, and M. Pejrup, “Turbidity, particle fluxes and mineralisation of carbon and nitrogen in a shallow coastal area,” *Marine and freshwater research*, vol. 46, no. 1, pp. 409–418, 1995.
- [2] A. Tengberg, E. Almroth, and P. Hall, “Resuspension and its effects on organic carbon recycling and nutrient exchange in coastal sediments: in-situ measurements using new experimental technology,” *Journal of Experimental Marine Biology and Ecology*, vol. 285-286, pp. 119 – 142, 2003. Benthic Dynamics: In-Situ Surveillance of the Sediment-Water Interface.
- [3] S. C. Wainright, “Stimulation of heterotrophic microplankton production by resuspended marine sediments,” *Science*, vol. 238, no. 4834, pp. 1710–1712, 1987.
- [4] G. Yahel, M. Gilboa, S. Grossbard, A. Vainiger, T. Treibitz, Y. Schechner, U. Shavit, and T. Katz, “Biological activity: an overlooked, mechanism for sediment resuspension, transport, and modification in the ocean,” in *Proceedings of Particles in Europe*, SEQUOIA, 2018.
- [5] R. Yahel, G. Yahel, and A. Genin, “Daily cycles of suspended sand at coral reefs: a biological control,” *Limnology and Oceanography*, vol. 47, no. 4, pp. 1071–1083, 2002.
- [6] G. Yahel, R. Yahel, T. Katz, B. Lazar, B. Herut, and V. Tunnicliffe, “Fish activity: a major mechanism for sediment resuspension and organic matter remineralization in coastal marine sediments,” *Marine Ecology Progress Series*, vol. 372, pp. 195–209, 2008.
- [7] T. Katz, G. Yahel, M. Reidenbach, V. Tunnicliffe, B. Herut, J. Crusius, F. Whitney, P. V. Snelgrove, and B. Lazar, “Resuspension by fish facilitates the transport and redistribution of coastal sediments,” *Limnology and Oceanography*, vol. 57, no. 4, pp. 945–958, 2012.
- [8] T. Katz, G. Yahel, R. Yahel, V. Tunnicliffe, B. Herut, P. Snelgrove, J. Crusius, and B. Lazar, “Groundfish overfishing, diatom decline, and the marine silica

- cycle: Lessons from Saanich Inlet, Canada, and the Baltic Sea cod crash,” *Global Biogeochemical Cycles*, vol. 23, no. 4, 2009.
- [9] G. Yahel, “Research related video and photos, Oceanography and Marine Biology.” <https://www.youtube.com/user/gitaiyahel/videos>.
  - [10] M. Gilboa, “Biological resuspension videos.” [https://www.youtube.com/channel/UCh3xzxT0truVnYKzG5\\_cUoQ/videos](https://www.youtube.com/channel/UCh3xzxT0truVnYKzG5_cUoQ/videos).
  - [11] M. Gilboa, T. Katz, U. Shavit, S. Grosbard, A. Torfstien, and G. Yahel, “Novel approach to measure the rate of sediment resuspension at the ocean and to estimate the contribution of fish activity to this process,” in *Proceedings of Particles in Europe*, SEQUOIA, 2018.
  - [12] K. Robert and S. Juniper, “Surface-sediment bioturbation quantified with cameras on the neptune canada cabled observatory,” *Marine Ecology Progress Series*, vol. 453, pp. 137–149, 2012.
  - [13] S. Villéger, S. Brosse, M. Mouchet, D. Mouillot, and M. J. Vanni, “Functional ecology of fish: current approaches and future challenges,” *Aquatic Sciences*, vol. 79, no. 4, pp. 783–801, 2017.
  - [14] A. K. Rai and A. Kumar, “Continuous measurement of suspended sediment concentration: Technological advancement and future outlook,” *Measurement*, vol. 76, pp. 209 – 227, 2015.
  - [15] S. Pinet, J.-M. Martinez, S. Ouillon, B. Lartiges, and R. E. Villar, “Variability of apparent and inherent optical properties of sediment-laden waters in large river basins—lessons from in situ measurements and bio-optical modeling,” *Optics express*, vol. 25, no. 8, pp. A283–A310, 2017.
  - [16] S. Shahi and E. Kuru, “An experimental investigation of settling velocity of natural sands in water using Particle Image Shadowgraph,” *Powder Technology*, vol. 281, pp. 184–192, 2015.
  - [17] C. Thompson, F. Couceiro, G. Fones, R. Helsby, C. Amos, K. Black, E. Parker, N. Greenwood, P. Statham, and B. Kelly-Gerrey, “In situ flume measurements of resuspension in the North Sea,” *Estuarine, Coastal and Shelf Science*, vol. 94, no. 1, pp. 77–88, 2011.
  - [18] D. C. Fugate and C. T. Friedrichs, “Determining concentration and fall velocity of estuarine particle populations using ADV, OBS and LISST,” *Continental Shelf Research*, vol. 22, no. 11-13, pp. 1867–1886, 2002.
  - [19] E. J. Davies, W. A. M. Nimmo-Smith, Y. C. Agrawal, and A. J. Souza, “Scattering signatures of suspended particles: an integrated system for combining

- digital holography and laser diffraction,” *Optics Express*, vol. 19, no. 25, pp. 25488–25499, 2011.
- [20] G. E. Elsinga, F. Scarano, B. Wieneke, and B. W. van Oudheusden, “Tomographic Particle Image Velocimetry,” *Experiments in Fluids*, vol. 41, no. 6, pp. 933–947, 2006.
- [21] X. H. Nguyen, S.-H. Lee, and H. S. Ko, “Analysis of electrohydrodynamic jetting behaviors using three-dimensional shadowgraphic tomography,” *Appl. Opt.*, vol. 52, pp. 4494–4504, Jul 2013.
- [22] M. Raffel, C. E. Willert, F. Scarano, C. J. Kähler, S. T. Wereley, and J. Kompenhans, *Particle Image Velocimetry: A Practical Guide*. Springer, 2018.
- [23] Y. Gim, D. H. Shin, D. Y. Moh, and H. S. Ko, “Development of limited-view and three-dimensional reconstruction method for analysis of electrohydrodynamic jetting behavior,” *Opt. Express*, vol. 25, pp. 9244–9251, Apr 2017.
- [24] A. Levis, Y. Y. Schechner, and R. Talmon, “Statistical tomography of microscopic life,” in *Proceedings of IEEE/CVF Conference on Computer Vision and Pattern Recognition*, pp. 6411–6420, IEEE/CVF, 2018.
- [25] A. Aides, Y. Y. Schechner, V. Holodovsky, M. J. Garay, and A. B. Davis, “Multi sky-view 3d aerosol distribution recovery,” *Optics Express*, vol. 21, no. 22, pp. 25820–25833, 2013.
- [26] M. Alterman, Y. Y. Schechner, M. Vo, and S. G. Narasimhan, “Passive tomography of turbulence strength,” in *Proceedings of European Conference on Computer Vision*, pp. 47–60, Springer, 2014.
- [27] V. Holodovsky, Y. Y. Schechner, A. Levin, A. Levis, and A. Aides, “In-situ multi-view multi-scattering stochastic tomography,” in *Proceedings of IEEE International Conference on Computational Photography*, pp. 1–12, IEEE, 2016.
- [28] T. Treibitz and Y. Y. Schechner, “Turbid scene enhancement using multi-directional illumination fusion,” *IEEE Transactions on Image Processing*, vol. 21, no. 11, pp. 4662–4667, 2012.
- [29] T. Treibitz, Y. Schechner, C. Kunz, and H. Singh, “Flat refractive geometry,” *IEEE Transactions on Pattern Analysis and Machine Intelligence*, vol. 34, no. 1, pp. 51–65, 2012.
- [30] Y. Y. Schechner and N. Karpel, “Attenuating natural flicker patterns,” in *Proceedings of MTS/IEEE OCEANS/TECHNO-OCEAN*, vol. 3, pp. 1262–1268, IEEE, 2004.

- [31] M. Sheinin and Y. Y. Schechner, “The Next Best Underwater View,” in *Proceedings of IEEE/CVF Conference on Computer Vision and Pattern Recognition*, pp. 3764–3773, IEEE/CVF, June 2016.
- [32] A. Vainiger, Y. Y. Schechner, T. Treibitz, A. Avni, and D. S. Timor, “Underwater Wide-Field Tomography of Sediment Resuspension,” in *Proceedings of Particles in Europe conference*, SEQUOIA, 2018.
- [33] N. G. Jerlov, *Optical oceanography*, vol. 5. Elsevier, 2014.
- [34] C. Mobley, E. Boss, and C. Roesler, “Ocean optics web book,” 2010. Available at <http://www.oceanopticsbook.info/>.
- [35] C. Moore, A. Barnard, P. Fietzek, M. R. Lewis, H. M. Sosik, S. White, and O. Zielinski, “Optical tools for ocean monitoring and research,” *Ocean Science*, vol. 5, no. 4, pp. 661–684, 2009.
- [36] “Coastal Wiki web page.” Available at [http://www.coastalwiki.org/wiki/Main\\_Page](http://www.coastalwiki.org/wiki/Main_Page).
- [37] Y. C. Agrawal, “The optical volume scattering function: Temporal and vertical variability in the water column off the new jersey coast,” *Limnology and oceanography*, vol. 50, no. 6, pp. 1787–1794, 2005.
- [38] P. Traykovski, R. J. Latter, and J. D. Irish, “A laboratory evaluation of the laser in situ scattering and transmissometry instrument using natural sediments,” *Marine Geology*, vol. 159, no. 1-4, pp. 355–367, 1999.
- [39] G. Voulgaris and J. H. Trowbridge, “Evaluation of the acoustic Doppler velocimeter (ADV) for turbulence measurements,” *journal of atmospheric and oceanic technology*, vol. 15, no. 1, pp. 272–289, 1998.
- [40] H. Chanson, “Acoustic Doppler velocimetry (ADV) in the field and in laboratory: practical experiences,” in *International meeting on measurements and hydraulics of sewers*, pp. 49–66, 2008.
- [41] U. Shavit, A. Halamish, S. Grossbard, S. Asher, M. Gilboa, T. Katz, and G. Yahel, “Testing a biological resuspension footprint model using Lagrangian simulations,” in *Proc. Particules in Europe*, SEQUOIA, 2018.
- [42] S. Grossbard, M. Gilboa, T. Katz, G. Yahel, and U. Shavit, “Developing a laboratory simulator for the study of resuspension events,” in *Proceedings of Particles in Europe*, SEQUOIA, 2018.
- [43] H. Maas, A. Gruen, and D. Papantoniou, “Particle tracking velocimetry in three-dimensional flows,” *Experiments in Fluids*, vol. 15, no. 2, pp. 133–146, 1993.

- [44] K. Ohmi and H.-Y. Li, “Particle-tracking velocimetry with new algorithms,” *Measurement Science and Technology*, vol. 11, no. 6, p. 603, 2000.
- [45] Q. Liao, H. A. Bootsma, J. Xiao, J. V. Klump, A. Hume, M. H. Long, and P. Berg, “Development of an in situ underwater particle image velocimetry (UWPIV) system,” *Limnology and Oceanography: Methods*, vol. 7, no. 2, pp. 169–184, 2009.
- [46] B. Wang, Q. Liao, J. Xiao, and H. A. Bootsma, “A free-floating PIV system: Measurements of small-scale turbulence under the wind wave surface,” *Journal of Atmospheric and Oceanic Technology*, vol. 30, no. 7, pp. 1494–1510, 2013.
- [47] B. Wang, Q. Liao, H. A. Bootsma, and P.-F. Wang, “A dual-beam dual-camera method for a battery-powered underwater miniature PIV (UWMPIV) system,” *Experiments in fluids*, vol. 52, no. 6, pp. 1401–1414, 2012.
- [48] Q. Liao, B. Wang, and P.-F. Wang, “In situ measurement of sediment resuspension caused by propeller wash with an underwater particle image velocimetry and an Acoustic Doppler Velocimeter,” *Flow Measurement and Instrumentation*, vol. 41, pp. 1–9, 2015.
- [49] C. Atkinson and J. Soria, “An efficient simultaneous reconstruction technique for tomographic particle image velocimetry,” *Experiments in Fluids*, vol. 47, no. 4-5, p. 553, 2009.
- [50] H. Maas, P. Westfeld, T. Putze, N. Bøtkjær, J. Kitzhofer, and C. Brücker, “Photogrammetric techniques in multi-camera tomographic PIV,” in *Proceedings of the 8th international symposium on particle image velocimetry*, pp. 25–28, 2009.
- [51] J. Klinner and C. Willert, “Tomographic shadowgraphy for three-dimensional reconstruction of instantaneous spray distributions,” *Experiments in fluids*, vol. 53, no. 2, pp. 531–543, 2012.
- [52] X. H. Nguyen, S.-H. Lee, and H. S. Ko, “Comparative study on basis functions for projection matrix of three-dimensional tomographic reconstruction for analysis of droplet behavior from electrohydrodynamic jet,” *Applied optics*, vol. 51, no. 24, pp. 5834–5844, 2012.
- [53] M. J. Sathe, I. H. Thaker, T. E. Strand, and J. B. Joshi, “Advanced PIV/LIF and shadowgraphy system to visualize flow structure in two-phase bubbly flows,” *Chemical Engineering Science*, vol. 65, no. 8, pp. 2431–2442, 2010.
- [54] B. R. Halls, D. J. Thul, D. Michaelis, S. Roy, T. R. Meyer, and J. R. Gord, “Single-shot, volumetrically illuminated, three-dimensional, tomographic laser-

- induced-fluorescence imaging in a gaseous free jet,” *Optics Express*, vol. 24, p. 10040, may 2016.
- [55] X. H. Nguyen, Y. Gim, and H. S. Ko, “Multifunctional, three-dimensional tomography for analysis of electrohydrodynamic jetting,” *Optics and Lasers in Engineering*, vol. 68, pp. 235–243, 2015.
- [56] L. Marchitto, D. Hampai, S. Dabagov, L. Allocca, S. Alfuso, C. Polese, and A. Liedl, “GDI spray structure analysis by polycapillary X-ray  $\mu$ -tomography,” *International Journal of Multiphase Flow*, vol. 70, pp. 15–21, 2015.
- [57] SEIKA Digital Image Corporation, “Particle imaging velocimetry concept visualization.” Available at [https://www.seika-di.com/en/measurement/principle\\_of\\_piv.html](https://www.seika-di.com/en/measurement/principle_of_piv.html).
- [58] LaVision Inc., “Tomographic particle imaging velocimetry.” Available at <http://lavision.de/en/>.
- [59] A. Levis, Y. Y. Schechner, A. Aides, and A. B. Davis, “Airborne three-dimensional cloud tomography,” in *Proceedings of IEEE International Conference on Computer Vision*, pp. 3379–3387, IEEE, 2015.
- [60] A. Levis, Y. Y. Schechner, and A. B. Davis, “Multiplescattering microphysics tomography,” in *Proceedings of IEEE Conference on Computer Vision and Pattern Recognition*, vol. 1, IEEE, 2017.
- [61] A. H. Andersen and A. C. Kak, “Simultaneous algebraic reconstruction technique (SART): a superior implementation of the ART algorithm,” *Ultrasonic imaging*, vol. 6, no. 1, pp. 81–94, 1984.
- [62] M. Kak, Avinash C. and Slaney, “Algebraic Reconstruction Algorithms,” in *Principles of Computerized Tomographic Imaging*, ch. 7, pp. 275–296, Society of Industrial and Applied Mathematics, Jan. 2001.
- [63] P. C. Hansen and M. Saxild-Hansen, “AIR tools—a MATLAB package of algebraic iterative reconstruction methods,” *Journal of Computational and Applied Mathematics*, vol. 236, no. 8, pp. 2167–2178, 2012.
- [64] “Modulation Transfer Function of a Tamron MTFM112F12.” Available at MU\_M112FM12\_E\_D012\_300mm.pdf.
- [65] M. Pharr, W. Jakob, and G. Humphreys, *Physically Based Rendering: From Theory to Implementation*. Morgan Kaufmann, 2016.
- [66] B. K. Horn and R. W. Sjoberg, “Calculating the reflectance map,” *Applied optics*, vol. 18, no. 11, pp. 1770–1779, 1979.

- [67] “Luminous Efficacy Table.” Available at <http://hyperphysics.phy-astr.gsu.edu/hbase/vision/efficacy.html#c1>).
- [68] “Data sheet UI-3260CP-C-HQ Rev.2.” Available at [https://en.ids-imaging.com/IDS/datasheet\\_pdf.php?sku=AB00696](https://en.ids-imaging.com/IDS/datasheet_pdf.php?sku=AB00696).
- [69] W. Jakob, “Mitsuba renderer,” 2010. <http://www.mitsuba-renderer.org>.
- [70] H. R. Gordon, O. B. Brown, and M. M. Jacobs, “Computed Relationships Between the Inherent and Apparent Optical Properties of a Flat Homogeneous Ocean,” *Applied Optics*, 1975.
- [71] C. D. Mobley, *Light and water: radiative transfer in natural waters*. Academic press, 1994.
- [72] Amazon, “Amazon Elastic Compute Cloud (Amazon EC2).” Available at <https://aws.amazon.com/ec2/>.
- [73] J. Amanatides and A. Woo, “A fast voxel traversal algorithm for ray tracing,” in *Proceedings of Eurographics*, 1987.
- [74] A. Almogi-Labin, R. Calvo, H. Elyashiv, R. Amit, Y. Harlavan, and H. Herut, “Sediment characterization of the israeli mediterranean shelf,” *Geological Survey of Israel Report GSI/27/2012 and Israel Oceanographic and Limnological Research Report H*, vol. 68, 2012.
- [75] G. Bradski, “The OpenCV Library,” *Dr. Dobb’s Journal of Software Tools*, 2000.
- [76] Agisoft LLC, 2016. AgiSoft PhotoScan Professional, Version 1.2.6. Retrieved from <http://www.agisoft.com/downloads/installer/>.
- [77] N. Otsu, “A threshold selection method from gray-level histograms,” *IEEE transactions on systems, man, and cybernetics*, vol. 9, no. 1, pp. 62–66, 1979.
- [78] W. Matusik, C. Buehler, R. Raskar, S. J. Gortler, and L. McMillan, “Image-based visual hulls,” in *Proceedings of ACM Internationl Conference on Computer Graphics and Interactive Techniques*, pp. 369–374, ACM, 2000.
- [79] S. G. Narasimhan, M. Gupta, C. Donner, R. Ramamoorthi, S. K. Nayar, and H. W. Jensen, “Acquiring scattering properties of participating media by dilution,” in *Proceedings of ACM Transactions on Graphics*, vol. 25, pp. 1003–1012, ACM, 2006.
- [80] A. Geva, Y. Y. Schechner, Y. Chernyak, and R. Gupta, “X-ray Computed Tomography Through Scatter,” in *Proceedings of The European Conference on Computer Vision*, pp. 37–54, Springer, September 2018.



תמונות שנרכשו בכל המצלמות עברו כל נקודת זמן שהיא; ב. לבצע שחזרים לאורך זמן; ו. ג. להציג תוצאות ולהשווות בין ציפויות סידמנט משתנות. לאור תוצאות הניסויים, השגנו תוקף אמפירי של השיטה המוצעת בתיזה. ברם, השיטה מושגת עבור הנחת פיוור יחד, במוגבלת גודל מסך התאורה של המערכת, ועל כך אני דנה בשלב התוצאות. בפרק האחרון אני מציגה ניתוח של יכולות ומוגבלות הגישה המוצעת, שאלות המתעוררות הן מתוך הנחת המודל והן מהאתגר בדימות תה ימי. ובסופה אני מציגה כיוני המשך למחקר פוטנציאליים.

ההרחה, אנו מחלכים את העומק האופטי לאורך קו הראייה של כל פיקסל. באמצעות עקרון הטומוגרפיה המופעל על העומקים האופטיים של כלל הפיקסלים הצופים על הענן, אנו משחזרים את מקדם ההנחתה של ענן המשקע בכל אלמנט נפחית של הענן. מקדם ההנחתה מומר לציפויו מסה של החלקיים, ובכך ניתן לשחזר את כמות המשקע המורחפת הכוללת, לאורך תהליך הרוחפת המשקע.

לאחר ההקדמה, אני מציגה סקירה כללית של עבודות קודמות. סקירה זו כוללת מדידות תת ימיות מקומיות של משקעים, שיטות חקר מעבדיות של זורמים וחלקיים, ובדיקות העוסקות בחישבה אטמוספרית ושחזר תלת-מימד של אירוסולים ועננים. מספר עקרונות אשר הוצגו בעבודות אלו שולבו בעבודתנו, כגון מודל השחזר המתמטי, כיון המערכת וחישוב הטומוגרפיה.

בחלק התיאורתי אני מציגה את מודל התמונה המתבסס על משוואת מעבר קרינה תחת הנחת פיזור יחיד. ההנחה תקפה במקרים בהם התוווק מכיל תרחיף דليل. תחת הנחת זו, מודל ההנחתה לנארו וקיים עבורו פתרון אלגברי לבניית שחזר עניי הסדימנט מתחת למים. לאחר מכן מוצג הקשר הפיזיקלי בין מקדם ההנחתה שחזר בתהליך הטומוגרפיה לבין ציפויו מסת החלקיים. באמצעות קשר זה ניתן להעריך את כמות המשקע המורחפת. בסוף הפרק מתוארת בקצרה השיטה האלגברית SART המשמשת בשיחורי טומוגרפיה מעותות מבטים, בדומה לשיטה המוצגת בתיאזה זו. בפרק הרביעי אני מתארת את תכנון המערכת האלקטרו-אופטי, המהווה את לב מערכת הטומוגרפיה. בתחילת הפרק מובאות הדרישות המרחביות והזמןיות של המערכת. על בסיסן מפורטים השיקולים האופטיים והנדסיים לבחירת רכיבי המערכת. סט רכיבי המערכת האלקטרו-אופטי כולל: מצלמות, עדשות ומקור תאורה.

בפרק החמישי אני מציגה את בוחינת המודל ושחזר עניי סדימנט באמצעות הדמיות מחשב. הדמיות מבוססת על מודל מונטה קרלו המדמה מעבר קרינה בתווך. הדמיות והשחזרים בשלב זה תרמו בו זמינות לשני תהליכי עיקריים של התיאזה. הראשון, הינו תכנון אופטימאלי של מערכת הדימות במסגרת תקציב נתון. באמצעות הנחירו סוגים הרכיבים האלקטרואופטיים, ונקבעו כמותם ומיקומם המרבי. השני, בניית תשתיות אלגוריתמית אשר במחילה נבחנו מיימוש ל-SART, וכן כיצד בסיס לעיבוד התמונות וחישוב השחזרים של ניסויי הטומוגרפיה בהמשך.

בפרק השישי אני מפורטת על תהליכי בניית מערכת הטומוגרפיה התת ימית והשיקולים ההנדסיים והפיזיקליים הנלוים לה. התהליכי כלל התקנת מרחתビת של המצלמות, ובנית מסך אשר ישמש כמקור התאורה. המסך ועוצמת התאורה תרמו הן לרכישת הנתונים והן לקליברציה ומיפוי תלת-מימד של המערכת. בנוסף, מותוארת המערכת לייצור עניי הסדימנט אשר שולבה וסוכרנה עם המערכת האלקטרואופטי. בפרק זה מפורטים האמצעים והשיטות אשר פיתחנו והשתמשנו בהם לצורך כיון, מדידה ובוחינה של ביצועי מערכת בניסויי הטומוגרפיה בפועל.

מערכת הטומוגרפיה הופעלה בבריכת מי ים יעדית הנמצאת בבית הספר למדעי הים על שם צ'רני, באוניברסיטת חיפה. ביצעו מספר ניסויי טומוגרפיה מוצלחים. היכולת לשולט ולתזמון את מרכיבי המערכת, וביצוע ניסויים באופן שיטתי אפשרו: א. לסנן

# תקציר

בעבודה זו אני מציגה גישה חדשה לגדנשטיינט לוטומוגרפיה ממוחשבת (CT) אופטית תתי-ימית המיעדת לחקר משקעים בים. משקעים בים (סdimנט) מכילים חלקיקים גדולים שונים אשר מקורם בסלעים שהתפרקו או מוחמירים אורגניים. למשקעים בים השפעה על תהליכי מרכזים בטבע לרבות איכות המים, פיזור מזחמים, ותהליכי ביוכימיים לדוגמא מהזרי מזון בהם מרכיבי בסיס משתפים בתהליך הפוטוסינטזה. הרחפה הוא תהליך שבו משקעים שהתיישבו קודם לכן על פני קרקעם הים מושעים מעלה אל עמודת המים. תופעה זו נצפית בעיקר חול תת ימי ומתרחשת כאשר זרמי קרקעית מגעים למהירות סף, כתוצאה מתהליכי פיזיקליים כגון גלים ורוחות; פעילות אנושית כגון דיג ועבודות הנדסיות בים; או פעילות ביולוגיות. הרחפות ביולוגיות מתרחשות כאשר דגים ובעלי חיים תרים אחר אוכל ומכסה ליד קרקעית הים.

קיים פער ידע לגבי קצב, התקופה, וגודל ההשפעה של הרחפות סdimנט ופרט ביולוגיות. יתר על כן, השפעת הרחפות הביולוגיות על תהליכי ביוכימיים תתי-ימיים אינה ידועה. לאחרונה פורסמו עבודות המראות כי הרחפה ביולוגית עשויה להיות משמעותית יותר, בגין התראחות תכמה של אירועים מסווג זה. למורת מחקר רב שנעשה, טרם נמצאו שיטות מוסכמתות למדידת הסdimנט שכן הין מוגבלות מבחינה זמנית ו/או מרחבית. מדידת אירועי הרחפה ביולוגיות מתוגרת אף יותר, שכן הינם ספורדיים בזמן ובמרחב ובעומקם אינם בהכרח תלויים במצב הים.

בעודה זו מציגה גישה חדשה לחישת סdimנט בים ותורמת למדידה, כימות ואפיון של הרחפות סdimנט. גישתנו כוללת מערכת אופטית תתי-ימית המעניקה מימד לחישה נוספת ומרחיבה את שדה הראייה של השיטות הקיימות בחקר משקעים ימיים. גישתנו אומדנת את כמות המשקע המורם מעל הקרקע ואת התפלגותו המרחבית-זמןית בתלת מימד, באמצעות טומוגרפיה ממוחשבת. בתזה זו אני מפרטת את עקרונות הגישה שלנו, התיאוריה עליה מבוססת הפתרון, סימולציות מחשב ותוכנו הנדסי של מערכת ההדמיה האלקטרור-אופטית, תהליכי עיבוד הנתונים ואמונות אמפירית של מערכת הטומוגרפיה.

מערכת הטומוגרפיה המוצגת א. צופה על נפח המים שמעל הקרקע, למרחק. ב. חשה אירועים של הרחפות סdimנט, ו. ג. מתחזרת את תרחיף המשקע באופן אלגוריתמי. ענן החול הנוצר, מצולם מכיוונים ומיקומים שונים, בדומה לטומוגרפיה רפואי. חלקיקי המשקע משפיעים על הקירינה המגיעה למכלמות, ובכך יוצרים את התמונות המתקבלות בפרשפטיות השונות. לעיבוד נתונים קל יותר, במהלך התפתחות הענן, הציורים מתבצעים כנגדי תאורה לבנה דיפוסיבית. על ידי מדידת עצמות הקירינה לפני ובמהלכו של תהליכי

## תודות

תודה מיוחדת נתונה לפרופ' יואב שכנה, על כך שמעבר להיותו מנהה, היה עבורי מנטור שהפך את הדרכם למאתגרת ומהנה יחד.

אני מודה לד"ר טלי טרייביץ' ואביעד אבני מבית הספר למדעי בית הספר למדעי הים ע"ש ליאון צ'רני באוניברסיטת חיפה, כמו גם לדוד טימור, על שיתופו הפעולה הפורה עם ותרומות הרבה לבניית מערכת הטומוגרפיה וביצוע הניסויים. אני אסירת תודה למי שסייע לבניית המערכת ובניסויים, מיכאל פישר, עידן צ'רנינסקי, יובל גולדפרקט, לאוניד דהטר, בן הרצברג, אסף לוי, ג'ודית פישר, פרופ' מורל גרופר, שמואל כהן ושרון פרבר. אני מודה לקולגות שלי על הדיוונים המפרטים במהלך התואר, ואדים חולזובסקי, אביעד ליס, ד"ר עמית איידס, ליאור ארבל, ד"ר מצדה צמח צברי ומארק שיינין מהמעבדה לדימוט היברידי, הפוקולטה לחשמל ע"ש אנדרו ואיירנה ויטרבי, הטכניון.

לקבלת תמיכה טכנית אני מודה לאינה טלמן ולヨוחנן ארץ מהמעבדה למדעי הראייה והتمוננה, ולרווי מיטרני מהמעבדה למערכות תוכנה מורשות, הפוקולטה להנדסת חשמל ע"ש אנדרו ואיירנה ויטרבי, הטכניון. אני מודה על הסיוע הטכני והציז שמשו אותי במהלך תהליכי הכיל והקליברציה של המשקעים מגליה בר-זוז, מהמעבדה להנדסת תא גע ורקבות, הפוקולטה להנדסה ביי - רפואי, הטכניון.

אני מודה על הדינאים המדעיים ושיתופו המידע הפורה עם ד"ר תימור צ' מהמכון הישראלי לחקר הימים והאגמים, לפרופ' גיתאי יהל ומירב גלבוע ממעבדת אוקיאנוغرפיה וביולוגיה ימית, המרכז האקדמי רופין, ולפרופ' אורן שביט ושהר גروسברד מהפקולטה להנדסה אזרחית וסביבתית, הטכניון.

המחקר לתזה זו נערך בעיקר במרכז Ollendorff Minerva, המרכז ממומן באמצעות BMBF. במהלך השתלים קיבلتם תמיכה כספית מהקרן הדגלומית למדע ארץות הברית-ישראל, BSF, מקרן מפ"א, וממשרד המדע, הטכנולוגיה והחלל הישראלי.

אני מודה לטכניון על התמיכה הכספית הנדיבה בהשתלמותי.

המחקר בוצע בהנחייתו של פרופסור יואב שכנר בפקולטה להנדסת חשמל על שם אנדרו  
וAIRNA ויטרבי.

### **פרסומים**

חלק מן התוצאות בחיבור זה פורסמו כמאמרים מאת המחבר ושותפיו למחקר בכנסים  
ובכתבי-עת במהלך תקופת המאסטר של המחברת, אשר גרסאותיהם העדכניות  
**ב尤תך הינן:**

- Adi Vainiger, Yoav Y. Schechner, Tali Treibitz, Aviad Avni, and David S. Timor,  
“Underwater Wide-Field Tomography of Sediment Resuspension”, in Particles in Europe conference 2018, (2018).
- Adi Vainiger, Yoav Y. Schechner, Tali Treibitz, Aviad Avni, and David S. Timor,  
”Optical wide-field tomography of sediment resuspension,” *Optics Express* 27,  
A766-A778 (2019).



# **טומוגרפיה תת-ימית של הרחפת משקע בשדה רחוב**

**חיבור על מחקר**

לשם מילוי תפקיד של הדרישות לקבלת התואר  
**מגיסטר למדעים בהנדסת חשמל**

**עדן ויינגר**

הוגש לסנט הטכניון --- מכון טכנולוגי לישראל  
תשרי התש"ט חיפה אוקטובר 2019



# **טומוגרפיה תת-ימית של הרחפת משקע בשדה רחוב**

**עדיו וויניגר**